2011

A Probabilistic Assessment of Vertebral Cortical Bone Fracture of Intraosteonal Structures

Isaac Graham Mabe
Wright State University

A PROBABILISTIC ASSESSMENT OF VERTEBRAL CORTICAL BONE FRACTURE OF INTRAOSTEONAL STRUCTURES

A thesis submitted in partial fulfillment
of the requirements for the degree of
Master of Science in Engineering

By

Isaac Graham Mabe
BSCE Ohio University, 2007

2011
Wright State University

WRIGHT STATE UNIVERSITY

GRADUATE SCHOOL

July 26, 2011

I HEREBY RECOMMEND THAT THE THESIS PREPARED UNDER MY SUPERVISION BY Isaac Graham Mabe ENTITLED A Probabilistic Assessment of Vertebral Cortical Bone Fracture of Intraosteonal Structures BE ACCEPTED IN PARTIAL FULFILLMENT OF THE REQUIREMENTS FOR THE DEGREE OF Master of Science in Engineering

Tarun Goswami, D.Sc.
Thesis Director

Thomas N. Hangartner, Ph.D.,
Chair Department of Biomedical,
Industrial & Human Factors
Engineering

Committee on
Final Examination

Tarun Goswami, D.Sc.

David B. Reynolds, Ph.D.

Chandler A. Philips, M.D., P.E.

Michael Herbenick, M.D.

Andrew T. Hsu, Ph.D.
Dean, Graduate School

ABSTRACT

Mabe, Isaac Graham. M.S. Egr., Department of Biomedical, Industrial and Human Factors Engineering, Wright State University, 2011. A Probabilistic Assessment of Vertebral Cortical Bone Fracture of Intraosteonal Structures

Cortical bone is a porous structure. The presence of these pores creates the possibility of a local overstressed area that has the likelihood of premature failure. Some failure modes of the vertebral endplates, for example subsidence which occurs at rates as high as 77 percent, can be better predicted with further understanding of failure mechanisms and the ability to predict those mechanisms. A probabilistic assessment of the pore size and its contribution to the fracture toughness has not been investigated in the cortical shell of the vertebral endplates. This research develops a probabilistic model that has the ability to determine the fracture toughness of a deterministic cortical bone sample versus the probability of exceeding the crack length that causes failure. Also the model can compare the crack size limit to the thickness of cortical bone present. The work presented is a novel approach to determining probabilistic fracture toughness of vertebral cortical bone.

TABLE OF CONTENTS

I. INTRODUCTION 1

II. LITERATURE REVIEW 4

A. CERVICAL SPINE ANATOMY 4

B. ANATOMY OF VERTEBRAL BODIES 12

C. BONE HISTOLOGY 20

III. PORE SIZE DISTRIBUTION 24

IV. BONE AS AN ENGINEERING MATERIAL 30

V. SUBSIDENCE AND VERTEBRAL BODY MODELING 34

VI. BONE FRACTURE MECHANICS 44

VII. PROBABILISTIC FRAMEWORK FOR EVALUATION OF TOUGHNESS OF VERTEBRAL CORTICAL BONE 52

VIII. RESULTS / DISCUSSION 69

IX. CONCLUSION 84

X. REFERENCES 86

XI. APPENDIX 97

CALCULATIONS 97

LIST OF FIGURES

1. Cervical Vertebra 5
2. Vertebral Body Architecture Comparison 13
3. Intervertebral Disc Loading Biomechanics 14
4. Hierarchical Bone Structure 21
5. Sagittal endplate section showing transverse osteon distribution. 26
6. Pores present in cortical bone, canaliculai highlighted 29
7. Vertebral Body Finite Element Model and Endplate Parameters 38
8. Mode I fracture opening in compact tension specimen 45
9. Load Diagrams, Load Case 1 and Load Case 2 56
10. Probability crack size less than limit length of beam Load Case 1 69
11. Probability crack size less than limit length of beam Load Case 2 70
12. Calculated Crack Limit per Beam Length, Load Case 1 71
13. Calculated Stress Intensity Factor, Load Case 1 72
14. Calculated Crack Limit per Beam Length, Load Case 2 72
15. Calculated Stress Intensity Factor, Load Case 2 73
16. Weibull Probability Distribution, Vashishth, Load Case 1 77
17. Weibull Probability Distribution, Dowling, Load Case 1 77
18. Weibull Probability Distribution, Feng, Load Case 1 78
19. Weibull Probability Distribution, Yan, Load Case 1 78
20. Weibull Probability Distribution, Vashishth, Load Case 2 79
21. Weibull Probability Distribution, Dowling, Load Case 2 79

22. Weibull Probability Distribution, Feng, Load Case 2 80

23. Weibull Probability Distribution, Yan, Load Case 2 80

24. Probability ‘a’ less then limit vs. specimen thickness, Load Case 1 81

25. Probability ‘a’ less then limit vs. specimen thickness, Load Case 2 81

26. Reduced span multiplier Yan model, Case 1 82

27. Reduced span multiplier Yan model, Case 2 83

28. Example Distribution of crack lengths 99

LIST OF TABLES

1. Ranges of Motion Cervical Spine 11

2. Average Endplate Thicknesses 16

3. Elastic Modulus and Hardness by Nanoindentation 31

4. Summarization of Elastic Moduli and Method of Investigation 33

5. Summarization of Yield and Ultimate Strength 33

6. Finite Element Model Properties 39

7. Max Stresses of Endplate and Core under Flexion/Extension Loads 40

8. Core and Endplate Flexion Extension Comparison 41

9. Vertebral Body Strain Percentages 42

10. Fracture Toughness and Strain Energy Release Rate Summary 50

11. Vertebral Endplate Thickness Data 53

12. Porosity Data 61

13. Diameter Data Generated From Porosity Data 61

14. Weibull Distribution input values and R^2 values 75

15. Data used to build normal distribution 99

Acknowledgments

I would like to thank my advisor Dr. Tarun Goswami for the opportunity to work on the material presented here. I am also grateful for the opportunity to advance the breadth of scientific and engineering knowledge. Dr. Goswami's expertise and support proved an invaluable resource. His interest and determination in this research was encouraging. I would also like to thank my fellow colleagues in the spine research group: Mbulelo Makola, Susan Hueston, Daniel Reese and Dr. Mary Blackmore. Their efforts and our common goal made the work interesting and incredibly rewarding.

Dedication

I would like to dedicate this thesis to my parents Ed and Mary Kay Mabe. This work would have not been possible if it were not for their support. The commitment to hard work and knowledge has been a lifelong lesson learned from their early and consistent example.

Chapter I - Introduction

The cervical spine is a complex section of the spinal column. It has several components that work together in unison to provide humans with a large range of motion [6,58-64] at the neck and protection of the spinal cord. The ability to assess the health and strength and mechanical properties [12-25, 28-32] of the vertebrae is a sought after goal of the medical community. Attempts have been made to assess the health and strength non-invasively [21]. This aids in the efficacy for the patient. Several studies have tried to link these non-invasive techniques to the strength of the vertebrae. These techniques are valuable. The purpose of this research is to expand the strength assessments to the area of toughness of cortical bone. Vertebral bone is hard to test because of the difficulty in removing and procuring samples, specifically the removal from the trabecular core.

A probabilistic assessment of the toughness was developed due to the porous crack prone nature of the cortical bone [66]. This research is based of porosity values collected from literature on representative samples of bone [8-11]. The porosity values were collected and compiled into a normally distributed sample of crack lengths. It was assumed that porous structures are consistent regardless of the location and that the porosity of the femur is consistent with the pore sizes of the cortical bone of the vertebral endplate. Several features create voids in cortical bone. These features include Haversian canals, Volkmann's canals canaliculai and randomly distributed porous voids.

The pores are naturally occurring phenomena. The type of voids considered in this research are the randomly distributed pores not associated with Haversian canals, Volkmann's canals or canaliculai. The average area of the pore size analysis was 19591 μm^2.

The presence of thecracks within a solid creates a stress raising situation in that the local stress is much higher than the average stress of the specimen. The stress at the tip creates a stress intensity that can be described as a stress intensity factor. The limit below which a crack does not grow is called the fracture toughness of a material. Several studies have investigated the limit of the fracture toughness of cortical bone [12-19]. There are two types of fracture toughness, longitudinal and transverse. The longitudinal fracture toughness limits deal with fracture along the length of the osteons in the longitudinal direction of bone. Typically in long bones this direction is parallel to the long axis of a long bone. In the case of irregular bones the direction may not be as clear. In the case of vertebral bone the longitudinal direction of the bone is parallel to the axial plane. This creates a scenario in which transverse fracture can be considered. Transverse fracture limits typically have larger values than longitudinal directions because the crack must travel around osteons. This research considers the transverse fracture toughness as the benchmark to compare to the generated stress intensity factor.

The research builds a framework for the development of a probabilistic framework for the incidence of surpassing the fracture toughness limit. The model consists of a beam bending model that places cracks in the tension region of the beam.

The beam however required depth definition. The definition was compiled from literature reviews of cortical bone thickness of the vertebral endplates [47,53-55]. The data was combined into an equation that was used to describe the thickness of beam of cortical vertebral endplate bone. The dimensions were used to develop stress values that were applied to the differential bone specimens.

The placed cracks were used to calculate the stress intensity values. Four models were developed from previous fracture studies. Three of these models Vashishth, Dowling and Feng considered compact section fracture. These models investigated the cracking at each individual differential compact slice of the beam. The fourth model was developed from a three point beam bending study performed by Yan. These models differed widely with respect to the shape function. The shape function utilized the distribution of crack sizes to place in the beam and was able to determine the probability of a crack being present that would make the specimen exceed the fracture toughness of cortical bone.

Ultimately this research develops the probability of a crack size being present that makes the specimen of bone surpass its fracture toughness. This research does not predict fracture or the reduction of strength due to the presence of the crack.

Chapter II – Literature Review

II A. - Cervical Anatomy/Kinematics/Biomechanics

The cervical spine consists of the seven most superior vertebrae of the spinal column. The cervical column has a natural lordic curve. This is a convex curve anteriorly of the cervical column. The cervical column serves multiple purposes. It supports the head and provides muscle attachments to move the head and neck and it also protects the spinal cord and allows nerves to enter and exit the spinal cord [57].

The first cervical vertebra, C1, is called the atlas. This vertebra is different from the rest of the column; it has a ring like structure [57]. The atlas directly supports the skull by way of the superior facets. The superior facets articulate with the occipital condyles of the skull. Anterior on the atlas is the anterior arch. The anterior arch articulates with the C2 or axis vertebra. Directly posterior of the anterior arch is the posterior arch. This arch offers protection to the spinal cord. Two transverse processes extend from each side of the atlas. These processes have holes in each which allow blood vessels, namely the vertebral artery, to the brain [57].

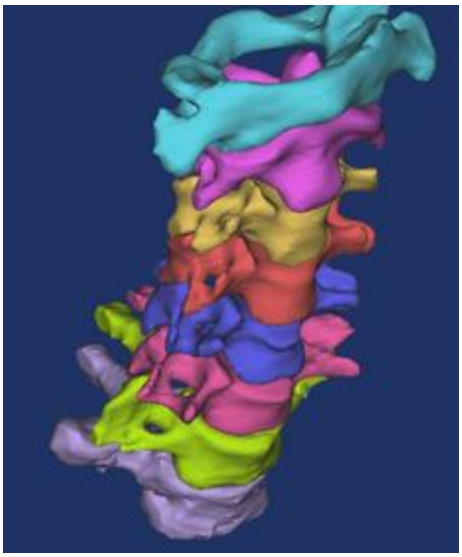

Figure 1. The cervical vertebrae from C1 through T1, 3D model developed with Mimics (Materialize, Ann Arbor Michigan).

The next vertebra down or inferior is the axis. The axis differs from the rest of the vertebrae and the axis. It consists of the odontoid or dens, this is a sort of body for the vertebrae. Unlike the C1 atlas the posterior arch is replaced by spinous processes which act as a protective device for the spinal cord and now offer a site for muscle and ligament attachment. The transverse processes continue in the axis as well as the rest of the way down the cervical column [57].

Another trend that continues down the column is facet articulation. Each vertebra has a superior articulating facet and an inferior articulating facet. The superior articulating facet interacts with the inferior articulating facet of the vertebrae above it, and the opposite holds going down the cervical column. The facets have approximately a 45 degree inclination that limits the extension and axial rotation of the cervical column [7].

Below the axis and atlas the cervical vertebrae are named C3-C7 in increasing order going down the cervical column. After C7 the thoracic region of the spinal column is reached and these vertebrae are called T1, T2, etc. C3-C7 all have the same general configuration. Anterior to the vertebra is a large bony structure is the vertebral body. It consists of a larger generally elliptical bony structure that articulates with the body directly above or below through a soft tissue structure called the intervertebral disc. The spinous processes continue down the posterior arch providing spinal cord protection and muscle and ligament attachment [56,57].

Between each vertebra is an intervertebral disc. The intervertebral disc is made from two parts, a nucleus pulposus and an annulus fibrosus. The nucleus is a gelatinous filled sac and the annulus is a concentrically layered ring of a cartilage like material. The biomechanics of the intervertebral disc will be discussed later. The main purpose of the intervertebral disc is to transfer axial forces through the spinal column and prevent individual vertebrae from rubbing against one another. When a two adjacent vertebrae and a disc are considered as a group it is called a functional spinal unit. The functional spinal unit is a plane or gliding type joint [57].

Several muscles attach to the cervical spine that creates motion of the head and neck. The primary flexors of the head and neck are the longus capitis and the rectus capitis anterior. Flexing is considered reducing the angle of the chin to the chest. When the same angle is extended the head and neck are considered extended. Extension is caused by the symmetrical contraction of the longissimus capitis, oblique capitis, rectus capitis posterior, semispinalis capitis, splenius capitis and the trapezius muscles. If the

extensors are flexed asymmetrically then the head and neck are subjected to a lateral bending motion that results in the ear of the tensed side being moved closer to its corresponding shoulder. That being said the sternocleidomastoid and the rectus capitis lateralis laterally flex the neck. If the sternocleidomastoid is symmetrically flexed then an extension rotation is formed [57].

Ligaments also play a necessary role in the cervical spine. Because the joint of the functional spinal unit is a gliding joint ligaments are required to aid in stability by limiting rotation of the joints. Two types of ligaments are present in the cervical spine in two groups the intrasegmental and intersegmental systems. The ligaments of the intrasegmental system include the ligamentum flavum, facet capsule, interspinous and intertransverse ligaments. The ligaments of the intersegmental system include the longitudinal ligaments and the supraspinous ligaments. To maintain stability the ligaments of the spine are pre-stressed (pre-tensioned). This occurs even when the functional spinal segments are in a neutral position [6].

Range of motion can be described as how much rotation or translation can be achieved in a certain direction. The ability for the joint to rotate or translate is known as degrees of freedom. In free space there are six degrees of freedom. There are three directions of translation, anterior/posterior, lateral and axial directions. Translation supplies three degrees of freedom or the ability to translate positively or negatively in each direction. Rotation supplies the remaining degrees of freedom. Around each axis of translation there is the ability to rotate. Positive rotation is considered counterclockwise around an axis and clockwise is considered negative rotation [1,2].

The interconnected segments of the spine allow for six degrees of freedom. At the atlanto-occipital joint (the base of the skull to C1 atlas) the only degree of freedom present is the rotation about the lateral directed vector. This means that the only motion permitted at this joint is flexion or extension of the head. These degrees of freedom allow the head to nod [56]. Impaction of bone features on one another limit the range of motion in flexion/extension.

The next spot of articulation sephalid is the atlanto-axial joint. The antlanto-axial provides much of the range of motion of the neck. The axis of rotation of the atlas is the dens of the axis. The facets between the atlas and the axis are biconvex. While the axis rotates the biconvexity allows slipping of the joint that decreases the joint spacing by nestling the atlas in the axis. When the rotation is returned to neutral the original height is returned [56]. The rotation at the joint is considered passive because the muscles creating the rotation attach to the head. The head then acts as the generator of the torque and the atlas acts as a washer. The atlanto-occipital joint transfers all this torque due to the sloped sides of the articulating surfaces. The limitations on flexion/extension are the bony impingement of the bony structures. The rotation limiter is the alar ligament or the capsules of the lateral atlanto-axial joints [56].

At this point, the inferior end of the axis, the regular morphology of the cervical spine is considered to begin. One exception is present however. The articulating facets take on slightly different angulations when viewed from a posterior caudal direction, viewing to a superior caudal direction. In the same view lower cervical spine facets are oriented in transversely [56] see figure 1.

From this point on the joint between the vertebrae act the same for the remainder of the cervical spinal column. The vertebral bodies exhibit an anterior lip that hangs down almost pointing in the inferior direction. In the posterior half of the vertebral bodies two uncinate processes are visible. If a slice were taken in the frontal plane the uncinate processes would be a convex curvature to the bottom of the vertebral body. If a slice were to be taken in the sagittal plane of the body the superior vertebrae a convex curvature would be present to the again the inferior direction of the body. When these two curvatures are oriented in the anatomic position it creates a saddle knuckle joint [56].

The facet joints play an important role in limiting extension of the joint. They also aid in limiting front to back translation. Also if there is rotation the facet limits rotation towards the direction of rotation. This is made possible by the approximate 45-degree angle orientation of the facets. The configuration of the cervical spine is much different than that of the other regions of the spine. The lumbar region has large flat endplates oriented almost perpendicular to each other as opposed to the saddle in the cervical spine. The thoracic region contains an additional set of processes that allow articulation with the ribs [57].

The cervical intervertebral disc is unique compared to the disc in the lumbar region. The annulus fibrosus is not present throughout the entire perimeter of the disc. The annulus fibrosus is concentrated most in the anterior medial directions. In the anterior position the fibers tend to orient medially in the intervertebral gap. In the posterior region of the vertebrae the annulus is represented by only a few annular fibers

oriented in the mid sagittal region of the vertebral body. Also present is an intervertebral cleft in the posterior of the vertebrae. The cleft is a fissure that separates the disc posteriorly creating a sort of rip in the transverse direction. The rest of the disc is the nucleus pulposus. The cleft formation in the posterior of the disc is a natural occurring phenomenon. The presence of the cleft allows the posterior portion of the vertebral body to glide about the anteriorly located axis. As the body swings around this axis it has the ability to ride up the uncinate process that was previously mentioned. The true form of constraint to this type of rotation is not currently known [56]. A summary of the range of motion is presented in Table 1.

Range of Motion (Degrees)									
		Boos, Aebi [6]	Galbuserra [64]	Wheeldon [63]	Penning, Wilmink [58]*	Aho [61]*	Bhalla, Simmons [62]*	Lind [59]*	Dvorak [60]*
C0-C1	Flex	25	-	-	-	-	-	-	-
	Ext	25	-	-	-	-	-	-	-
	Axial	5	-	-	1	-	-	-	-
	Lat	6	-	-	-	-	-	-	-
C1-C2	Flex	19	-	-	-	-	-	-	-
	Ext	19	-	-	-	-	-	-	-
	Axial	5	-	-	40.5	-	-	-	-
	Lat	40	-	-	-	-	-	-	-
C2-C3	Flex	10	-	5	-	12	9	10	10
	Ext	10	-	9	-	12	9	10	10
	Axial	11	-	-	3	-	-	-	-
	Lat	4	-	-	-	-	-	-	-
C3-C4	Flex	16	-	5	-	15	15	14	15
	Ext	16	-	8	-	15	15	14	15
	Axial	12	-	-	6.5	-	-	-	-
	Lat	7	-	-	-	-	-	-	-
C4-C5	Flex	20	-	5	-	22	23	16	19
	Ext	20	-	7.5	-	22	23	16	19
	Axial	12	-	-	6.8	-	-	-	-
	Lat	7	-	-	-	-	-	-	-
C5-C6	Flex	20	9.5	5	-	28	19	15	20
	Ext	20	8.3	10	-	28	19	15	20
	Axial	9	5.5	-	6.9	-	-	-	-
	Lat	7	9.6	-	-	-	-	-	-
C6-C7	Flex	17	-	6	-	15	18	11	19
	Ext	17	-	8	-	15	18	11	19
	Axial	8	-	-	2.1	-	-	-	-
	Lat	6	-	-	-	-	-	-	-

Table 1: Ranges of motion of vertebral segments. Ranges of motion were collected by either biomechanical testing or finite element analysis,'*' indicates information summarized by Bogduck [56].

II B. - Anatomy of the Vertebral Bodies

The structure of the cervical vertebra can be divided into a hierarchical structure. The structure is divided hierarchically in the sense that the different parts of the body have different material properties based on region specific architecture. The vertebral body is the anterior region of the cervical spine. Specifically the vertebral body has a cancellous core region, and cortical shell region and cartilaginous endplates. Biomechanically the vertebral bodies are responsible for the transmission of axial loads (compressive) down the spine [6].

The primary function of the cancellous core is the transmission of axial loads [6]. This load is partially shared by the cortical shell [44- 47]. Because the cancellous core transmits axial loads the trabeculae are oriented in a predominantly axial direction. The strength of the core is based on the length scale of the trabeculae and the amount of cross-linkning or trabecular connectivity [47]. Studies have tried to examine the effects of various parameters to describe the strength of vertebral bodies.

As stated previously trabecular bone is oriented along the lines of stress and the vertebral body transmits axial loads therefore one expects most of the trabeculum to be ordered in that direction. It has been shown that 70% of the bone volume of the trabecular core is oriented in the axial direction [66]. This same study showed that 50% of the longitudinal oriented trabecular bone yielded while under compressive loading [66]. This indicates that the vertically oriented bone acts like columns in a building and

that the horizontally oriented bone acts like horizontal braces to those columns. The more bracing the more load carrying capacity the vertical columns can carry (1,2).

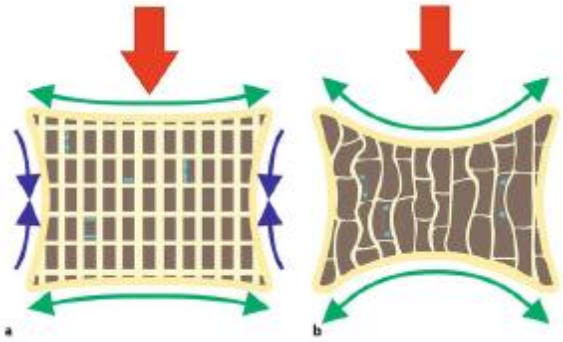

Figure 2: The left figure is a diagram of a healthy vertebra with greater connectivity between vertical trabeculae provided by the horizontal trabeculae. The figure on the right has reduced horizontal trabecular connectivity, the later results in less vertical support of the cortical endplates [6].

Further studies have shown described regional variation of trabecular bone within the vertebral body [47]. The posterior regions of the vertebral body had the greater bone volume, trabecular connectivity, more trabeculae, reduced trabecular and more plate-like than rod-like structure [47]. Based on Wolf's law this would indicate that most of the load carrying of the vertebral body is through the posterior areas of the vertebral body.

The cortical shell as described previously is a denser form of the cancellous core. There is a cortical shell that wraps radialy around the cancellous core. This offers the trabecular core support and load sharing. A very important part of the vertebral body structure is the superior and inferior vertebral endplates. The function of the endplate is to act as a boundary preventing the intervertebral disc from herniating into the vertebral body. It also acts like as a way to distribute loads evenly over the trabecular core. The bone is approximately a half-millimeter thick; the thickness of the bone will be

discussed in later sections. It also has a dense layer of cartilage between the bone and the disc to act as an attachment point for the intervertebral disc [6].

The load that is transferred to the endplate from the intervertebral disc is complex. The annulus of the disc acts as like a balloon and the nucleus acts like the air in the balloon.

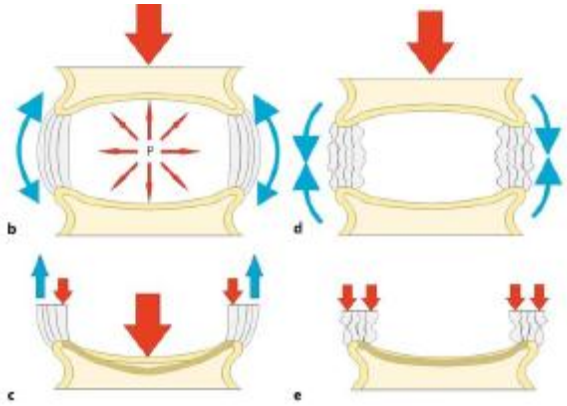

Figure 3: The figure on the left depicts a young healthy intervertebral disc that pressurizes the nucleus creating tension regions in the endplates. The right is an older disc that compresses the endplates in the region of the annulus ring [6].

As a pressure load is applied to the disc the nucleus hydrostatically pressurizes creating a tension region in the annulus and in the regions attached to the endplate. The hydrostatic characteristics of the disc cause a region of tension in the adjacent endplates [6,7].

The endplate role is very important to the health and strength of the disc. The porosity of the endplate allows a transfer of water to and from the disc. This aids in regeneration and health of the disc. When the body ages the porosity is thought to increase allowing more water to transfer out of the disc. This loss of water reduces the

amount the height of the column and reduces the amount of tension that goes to the vertebral body and turns the load into a more compressive load [6].

The strength and deflection of the vertebral body play a very important role in disc biomechanics. This is particularly important when the disc is removed and replaced. A replacement removes the disc in most cases and places some sort of fusion or disc replacement device. This changes the biomechanics to a compressive force with higher than normal contact forces [45,68].

To understand the endplate biomechanics the first thing that must be understood is the morphometry of the endplate. The thickness is one of the most important characteristics. Thickness drives stiffness parameters and determines other variables like the moment of inertia of the endplate in bending conditions. Several studies have been looked at the thickness of the endplate and stiffness of the endplate [25,41]. Variation is common from person to person however general trends in regions of thickness can be found.

Overall variation in endplate thickness has been measured as thin as 0.35 mm in the central regions of the endplate to as large as 1.2 millimeters toward the periphery of the endplates. Consistently the posterior region of the superior endplate has been the thickest region while on the inferior region it is the anterior portions of the endplate. This holds true for the cervical spine and for much of the thoracic and lumbar spine [8,47,53-55]. Table 2 summarizes endplate thickness values.

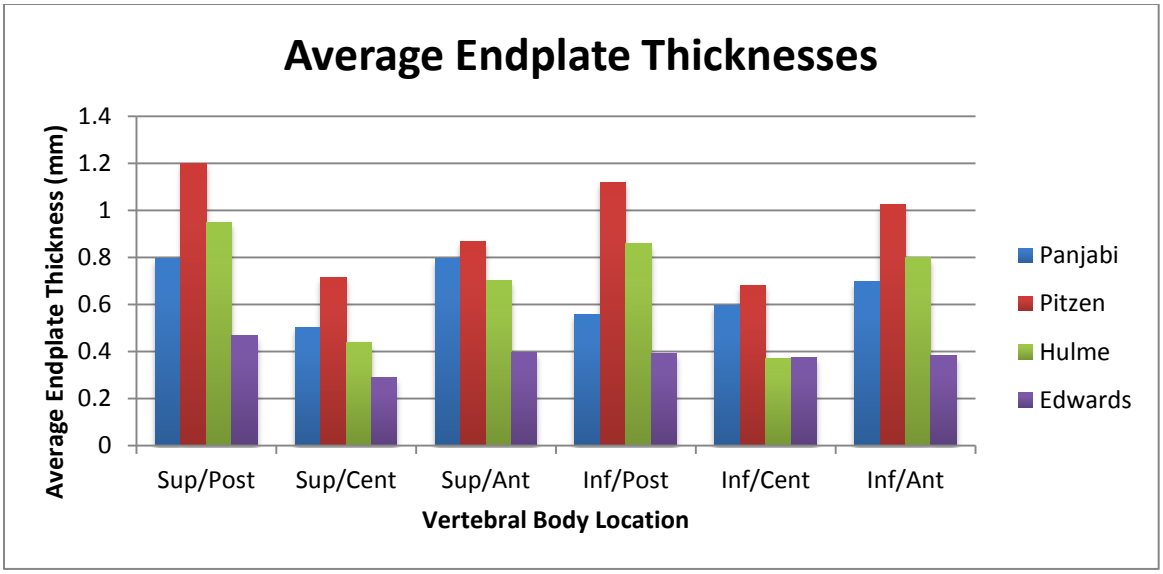

Table 2: Average endplate thicknesses of the inferior and vertebral endplates (combined) in the midsagittal plane.

From the collected data above the central regions of the endplate are the thinnest therefore would have the weakest mechanical properties. The thickness is an important consideration for orthopedic applications. Being aware of the thickness distributions allows placement criterion to be developed for intervertebral devices. Ideally implanted devices should bear on the strongest areas of the endplate that according to classic mechanics of materials would be the thickest parts.

Loading interaction between the cortical endplate and the trabecular core has been an area of much interest. It is difficult to determine just how strong the endplate is because harvesting it would almost certainly destroy the bony tissue. The tissue would also be almost too thin to test in a reliable and repeatable manner. Typically Finite element methods are used to determine the strength of the endplates [44,45,51,67].

Before an endplate is removed indentation tests can be used to determine the stiffness of the endplate/cancellous core combo [41]. Typically indentation tests are

mapped out over the surface of a vertebral endplate. The lumbar region of the spine was tested for stiffness (units of N/mm). In the anterior/posterior direction the highest stiffness was in the posterior rim of the endplate towards the periphery. Averaged over the entire posterior region however the stiffness was about 100 N/mm as compared to the anterior position that was 130 N/mm (Grant 01). Laterally across the vertebral body the lateral peripheries were stiffer that the central regions. This trend held for the superior and inferior endplates. The average stiffness on the endplate periphery was about 120 N/mm and in the center it was about 70 N/mm. The inferior endplate, at least in the lumbar region, was stiffer. Values were about 165 and 95 N/mm for the averages of the periphery and the center respectively [41]. These experiments show how the vertebral body reacts to very specific loading conditions, specifically indentation testing.

Indentation testing is destructive and requires cadavers. Its applicability per patient information would be best used correlated to other factors in the vertebral endplate. The most illustrative mapping of cervical vertebral endplate thickness measured the endplate in a radial fashion that gave a highly detailed map of thicknesses [53]. Measurements were taken in all directions in several locations of the vertebra and a large sample size, 24 individual vertebrae, was measured. Consistent among all vertebrae was a thick periphery and a thinner middle. The periphery thickness was on the order of about 0.8 – 1.15 mm thick while the central region was on the grouped at about 0.7 -0 .8 mm. As previously stated the central regions of the vertebral endplate had lower stiffness values than the periphery according to indentation testing [41].

Mineral density was investigated on the cervical vertebral endplates [42]. Regions of higher mineralization, or denser bone, have been known to reflect long-term stress distributions. Overall, the periphery of the endplates had the highest mineralization ($p<0.0001$) with the central regions having a lesser degree of mineralization. Results of the mineralization study showed that for superior endplates the posteromedial region had high mineralization. The inferior endplate regions of high mineralization tended to be in the anteromedial region. Coincidentally the same regions have the highest stiffness values as measured by indentation. The denser regions of higher mineralization also happen to be in thicker areas as well. The conclusion of the study conducted by Muller-Gerbl was that regions that exhibited long-term higher loads correlated to denser regions with higher mineralization, thicker regions and mechanically stiffer regions based on indentation tests [42]. These correlations held true for both the superior and inferior endplates.

Another study performed by Ordway [40] sought to investigate the preoperative strength of cervical subchondral bone by means of CT imaging. The CT imaging was correlated to indentation testing to create a basis for strength assessments. Regional yield loads and stiffness were measured in the tests with an intact endplate. The trabecular bone density directly beneath the endplate was measured for density. The yield load ranged from 120 ± 62 to 161 ± 84 N. The stiffness ranged from 134 ± 47 to 175 ± 66 N/mm. Again the yield loads and the stiffness were greatest in the thicker posteromedial region. The trabecular density varied under the endplate. The peripheral quantitative computed tomography (pQCT) results showed that there was increasing

trabecular density under both the higher yield region of the endplate and stiffer region of the endplate. The correlation was relatively low though with R^2 values of 0.37 and 0.42, respectively.

The previously mentioned studies both show the same relationships between stiffness in the posteromedial regions. If all the other correlations were to hold true then it is reasonable to conclude that the endplate is less dense in its thinner regions [84]. These studies lack fracture properties of the bone and also how the crack distribution weakens the endplates.

II C. - Bone Histology

Material strength and response to loads is a property inherent to the microstructure of said material. Classic materials like steel and aluminum are typically homogenous and isotropic. Homogenous meaning that the material is the same from point to point [1,2,5]. Isotropy means that a material's mechanical properties are the same in all directions [1,2,5]. A material's response to loads is a reflection of these inherent properties. Classic materials like steel or aluminum are typically homogenous and isotropic. From point to point the microstructure of homogenous and isotropic metals is the same.

Bone does not exhibit these same properties of homogeneity and isotropy. To understand bone it is important to understand what it looks like on a small scale. Physiologically bone is made of a matrix and bone cells. The bone matrix is composed of both an inorganic and organic material. The organic material is collagen and protoglycans. The inorganic material is hydroxyapatite. The combination of the two acts as a two phase reinforced material where the collagen acts like the flexible reinforcing and the hydroxyapatite acts as the rigid mineral component [57].

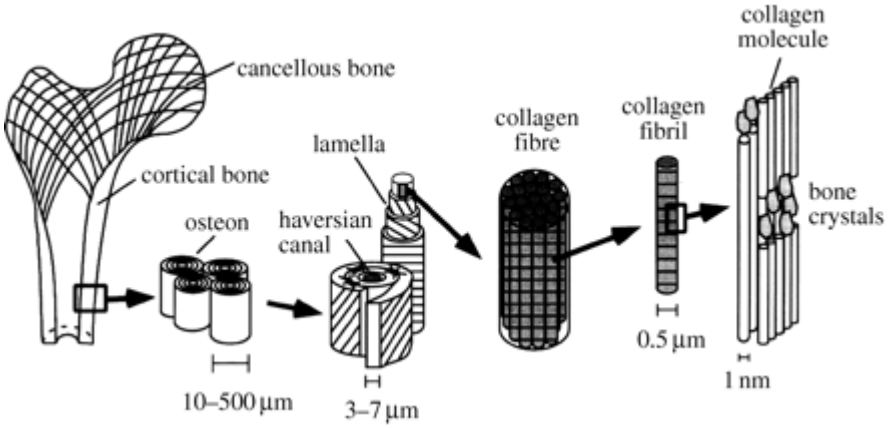

Figure 4. Hierarchical structure of bone from nano to macro level [65].

Because bone is a physiologic material, it has to regenerate. To regenerate the bone must use cells to build and resorb or destroy it. Osteoblasts are the delivery cells that provide collagen and protoglycans. The osteoblasts also concentrate calcium and phosphate that form hydroxyapatite crystals that further mineralize and promote hydroxyapatite formation. As the bone forms it creates outwardly growing concentric layers much like that of a tree. A new ring forms on top of the old layer [57].

As the bone matrix forms around the osteoblast it forms an osteocyte. At this point the cell is a mature bone cell and becomes inactive. A gap is formed between the osteocyte and bone matrix called lacunae. Individual osteocytes have the ability to communicate with adjacent osteocytes via processes called canaliculi. These canals like structures pass nutrients from one osteocyte to another [57].

The final type of bone cell is the osteoclast. Osteoclasts are responsible for bone resorption or the breakdown of bone. These cells cause the bone to decalcify and also produce an enzyme that digests the protein components of the matrix [57].

In adults bone is distributed into layered sheets called lamellae. The deposition of these lamellaer sheets affects the way the collagen fibers are oriented and ultimately controls the material properties of bone. In the same sheet collagen typically orients in the same direction however between sheets there is likely a change in angle of the fibers. Fiber orientation distribution is the primary driving force behind the anisotropic behavior of bone. If load is applied in the same direction to two different sheets of bone with their fibers oriented in two different directions the deflection of the bone is altered [57].

Bone deposited in the body comes in two forms; trabecular/cancellous or compact/cortical bone. The difference between the types of bone is the relative density of the bone. Cancellous bone is less dense than cortical bone. The bone itself is not different there just happens to be much more void space in cancellous bone. Cancellous bone is distributed in long rod-like structures. The rod-like structures grow and connect randomly throughout its volume of bone. Cancellous bone has the ability to change its distribution. This is an adaptive feature that gives it the ability to grow along lines of highest stress through the overall bone [57].

Cortical bone is denser than cancellous bone. Cortical bone also differs in that blood vessels are present in cortical bone. The blood vessel runs parallel to the long axis of the bone. These blood vessels are located in the center of concentrically deposited lamellae bone tissue called osteons. In the center of the osteon is what is called a Haversian canal that contains the blood vessels. The vessels distribute nutrients to the bone tissue. Osteons closely packed and there are several present in a very small space.

The diameter of an osteon is on the order of micrometers. Cortical bone has the ability to remove waste as well through a network of Volkmann's canals that run perpendicular to the long axis of a bone [57].

The previous description is basic to bones in general. This does not mean that all bone is created equal. There are different categories of bone; long, short, flat and irregular. Vertebral bone is of particular importance and is considered an irregular bone [57].

Chapter III - Pore Size and Distribution

Bone's material properties are affected by the distribution of voids. If bone were homogenous then classic equations of stress and deflection would apply to determine the strength of bone on the macro scale, or measurements on the order of millimeters. However the amount and size of micrometer sized pores affect bone's strength. The first goal is to understand how the physiologic structure of bone contributes to its porosity distribution and the size of the distributed pores.

Bone porosity and density have been studied in an attempt to indirectly determine its strength [9,10,11,42,47]. This review is particularly interested the cortical shell of a cervical vertebral body. The overall strength is difficult to quantify because there are many factors which affect the strength not to mention the complex load sharing that occurs between the cortical shell and the cancellous core.

Homminga reported that load is not shared evenly through the vertebral body [68]. At the superior and inferior endplates most of the load is carried by the trabeculae, approximately 95 percent. Towards the middle of the vertebral height the trabeculae of healthy vertebrae carries approximately 60 percent of the load [68]. The vertical trabeculae were the most strained at ±750 μm. Horizontally the trabeculae were less strained at ±50 μm [68]. Without a radial strain analysis of the cortical shell it can be assumed that the cortical shell acts as a restraint of the trabecular core.

The findings in the study by Homminga et al. are consistent with those of Eswaran et al. [45,46]. Eswaran found that the trabecula near the endplate was much more likely to be at high risk strain than at the mid-height of the vertebrae.

To identify bone porosity it is necessary to first identify what makes the bone porous. As mentioned before, there are several sources of porosity in bone. The Haversian canals, Volkmann's canals, canaliculai form areas of voids within the bone matrix. What were not mentioned were other random pores within bone. These areas are filled with some sort of fluid. In the case of Haversian canals blood fills the holes. Canaliculi and other voids are also filled with fluid.

Femurs have been used to analyze porosity using modalities such as microcomputed tomography (μCT) and low field pulse nuclear magnetic resonance (NMR). The findings of these studies are typically compared to histologic studies to verify the method of collecting information. The histologic measuring technique is the only direct way to measure porosity at a given surface of bone. The other methods are an attempt to develop a non-invasive way to determine bone porosity. It would be ideal to measure the actual porosity of cervical vertebral bodies; however, no such studies have been conducted on the investigation of porosity of the cortical bone of vertebral bodies.

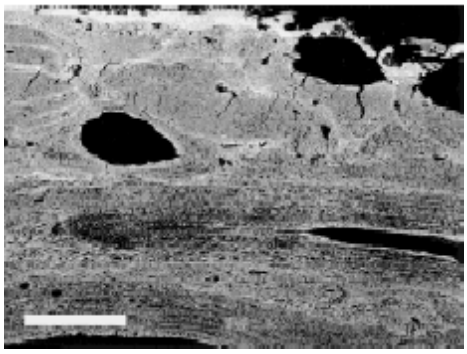

Figure 5. Sagittal endplate section scanned via backscattered electron micrograph [65].

Several methods have been used to collect porosity data. Haversian canal diameter is of particular interest due to the nature of trabecualrization and increases with age [9]. The study divided the femur into four sections anterior, posterior, superior, and inferior sections. The Haversian canal size, density and porosity were measured. The total number of canals per femur averaged 65,574 [9]. Canal sizes were also broken down into ranges. A large canal group ranged from 82-172 micrometers, an extra-large group was measured between 172-385 micrometers, and finally a large group was measured above 385 micrometers. These ranges were decided based on the size of the canal and the contribution to cortical porosity. It was found that 90 percent of the canal diameters fell in the large group, 7.5 percent fell in the extra-large group and 2 percent fell in the giant group [9].

The density of the canals ranged from 17.1 mm^2 to 20.4 mm^2. The mean canal diameters ranged from 49.4 mm to 60.2 mm. The median canal diameter was 38.3 to 45.3 mm. Overall the porosity range was from 41 to 57 percent.

Another example of indirect measuring of porosity is via microcomputed tomography (μCT). Again intracortical porosity was being examined as a way to

determine cortical strength. Osteons were also counted and measured. The μCT-scanned measurements were cross-referenced with histologic measurements to verify the accuaracy of the scanned measurements [11]. Haversian canals of osteons were considered closed systems in the cortical bone for this analysis. The analysis considers that porosity measurements as the available cracks.

The average haversian canal area was 4156.9 μm^2 with a range of 665-31244 μm^2. The osteonal area averaged an area of 41620.5 μm^2 with a range of 26390-63959 μm^2. Also measured was the area of bone porosity not associated with the haversian canals. The average area of porosity was 19862.5 μm^2 with a range of 3100-101337 μm^2. The average sizes show that the largest contribution to bone voids is the porosity however the pores may not necessarily be the largest voids. Total histogram porosity per specimen was found to average 9.1 percent. Osteons accounted for 41.6 percent of the total cross sectional are of the bone sample. The pore structures were also found to average 5.3 percent of a representative area of bone [11]. As stated before Haversian canals are not the only ones that contribute to the porosity in a cortical bone. The canaliculi lacunae also increase porosity of bone. Again the samples were analyzed histologically to verify the results [10].

Using the NMR approach to analyze the pores yielded interesting results. It showed that pore size and volume distributed into two main groups. The information was collected and analyzed using a log scale on the nominal pore size. In the log domain two distinct groups formed, one around a pore size of about 8-10 μm and another with a pore size on the order of about 100 μm. The two groups corresponded to lacunae and

haversian canals, respectively. A regression analysis of the NMR pore sizes vs. the histologic pore size indicated an 89 percent relationship, i.e. P_{hist} = .89*PNMR. The findings of this study show that the diameter of the haversian canals averaged 57.9 μm. The diameter of the lacunae averaged 3.87 μm [10].

The three previous studies all indicate that as people age the porosity of the cortical bone increases. The mechanism of increasing porosity has been observed as an increase in the size of the haversian canal within the osteon. The osteon itself may also increase in size but the haversian canal increases with age. The reduction is due to the case that the area is a function of the radius squared. So if the radius of the canal increases and the osteon remains relatively constant than the porosity is increased.

Considering the haversian canals in terms of diameters and radii is not necessarily correct. The canals are made up of irregular closed shapes. They could be considered more elliptical in shape than circular. However, describing a void in terms of a hemisphere is sufficient in determining the size of pore relative to other pores and can be used to describe distribution of those pore sizes.

This study will consider the crack openings that originate from porosity between the osteon canals. A pure tension situation or Mode I fracture is considered. The fracture caused by the haversian canals is product of a different type of opening mechanism than investigated here. The cracks may arise from a pure tension situation however the model is not the same. The completely enclosed crack case arises from cracks existing on the periphery of the canal radiating outward. Haversian canals would arise from open voids within a specimen. An assumption would have to be made that at

the inside perimeter of the haversian canal that a small crack would be present. This crack would likely be provided by the presence of canaliculi that provide communication pathways between adjacent osteon strands.

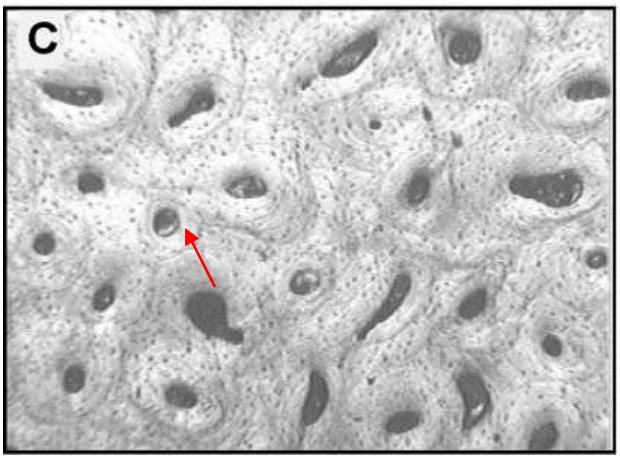

Figure 6. Picture of canaliculai highlighted by red arrow, one possible pore structure [10].

Chapter IV - Bone as an Engineering Material

Bone strength itself plays a very important role in the resistance to deformation and stress distribution. Individually, fiber-to-fiber bone exhibits the same elastic modulus. The elastic modulus is one of, if not, the most important characteristics of a material behind its yield strength. Studies have been performed on individual osteons. While this is important, osteons exist on a very small scale. Due to the shear non-homogeneity and anisotropy of bone hierarchical differences in bone behavior are present. They can be roughly categorized as cortical and trabecular with the only difference being the global density.

Basic mechanical properties of bone are derived from the osteonal structure. Biewener [20] studied the strain characteristics of cortical bone. One of the limitations was that only the outer layer of cortical bone could be measured and not to failure in vivo [20]. Several in vivo strains were measured and compared to failure strains that the cortical bone would see. Failure strain of vertebrate animals was recorded at -14000 to -21000 microstrain in compression. Compressive yield strain was also measured at -6000 to -8000 microstrain. In vivo tensile and shear yield strains were found to be 50-75% and 10-20% ,respectively. These values were measured on long bones.

Nanoindentation has also been used as a way to measure material properties of bone. Specifically the elastic modulus can be calculated from the indentation testing. The area of the indenter, the elastic modulus and poisson's ratio of both the indenter

and the indented must also be known along with the contact stiffness [22]. The equation to determine the elastic modulus from the stiffness calculations is

$$S = \frac{2}{\sqrt{\pi}} \beta \left(\frac{1-\nu_b^2}{E_b} + \frac{1-\nu_i^2}{E_i} \right)^{-1} \sqrt{A} \qquad \text{(Eqn. 1)}$$

Where: S = stiffness

β = constant

ν = poison's ratio

E = Modulus of elasticity

A = Area of indentor

The femur cortical and trabecular bone was tested in both the longitudinal and transverse direction. The results of the nanoindentation tests were as follows:

	Mean Elastic Modulus, GPa (S.D.)	Mean Hardness MPa (S.D.)
Trabecular –Transverse	13.4 (2.0)	468 (79)
Cortical Osteons – Longitudinal	22.5 (1.3)	614 (42)
Cortical Interstitial Lamellae – Longitudinal	25.8 (0.7)	736 (34)

Table 3: Elastic modulus and hardness values determined by nanoindentation [22].

From the above data the average mean elastic modulus of cortical bone with respect to osteons in the longitudinal direction is 22.5 GPa. This is higher than the widely accepted value of the elastic modulus for cortical bone of 18 GPa. The trabecular bone in this case is also measured at 13.4 GPa in the transverse direction.

These values obtained from various types of testing, i.e. nanoindentation, investigate what the mechanical properties of bone are on a microscale. On the continuum scale geometric effects reduce the effective stress, yield and ultimate strength of a material. For example Kopperdahl [31] examined the yield and ultimate stress in compression and tension of cylinders of trabecular bone. The average yield and ultimate strength in compression was 1.92 and 2.23 MPa, respectively. With respect to yield stress the average values were 1.75 and 1.33 MPa respectively. This is more relevant to trabecular bone that has larger differences point to point in its matrix than cortical bone. To a lesser extent this would hold true for cortical bone as well due to pore sizes and osteon boundaries.

Tensile testing performed by Bayraktar [23] reveals that cortical bone exhibits a range of elasticity that correlates to vascular porosity ($p<.001$). A cortical tissue (zero porosity value) value was calculated using the equation developed by a linear regression. The elastic modulus from a sample with zero porosity would be 19.9 GPa. Yield stress was also investigated from the tests. The values for compression and tension were 133.6 and 82.8 MPa, respectively.

Several tests have been used to establish elastic modulus properties and yield stresses in both compression and tension of cortical and trabecular bone. There is a wide variety of methods of analysis the results vary with several parameters including age and the health of the donor. A list of mechanical properties is provided. This list is not complete but thoroughly compiled.

Reference	Region	Method	Elastic Modulus (GPa)
*Ulrich[24]	Femur Head	Experimental – FEA	3.5-8.6
Rho[22]	Vertebral Trabeculae, Transverse	Nanoindentation	13.4
	Tibia Osteon – Longitudinal	Nanoindentation	22.5
	Tibia Lamellae – Longitudinal	Nanoindentation	25.8
*Hou[25]	Vertebrae	Experimental – FEA	5.7
*Ladd[26]	Vertebrae	Experimental – FEA	6.6
*Turner[29]	Distal Femur	Nanoindentation	18.1
*Zysset[30]	Femur Neck	Nanoindentation	11.4
*Niebur[27]	Bovine Tibia	Experimental – FEA	18.7
Bayraktar[23]	Femur Neck	Experimental – FEA	18.0
Roy[28]	Endplate – Coronal	Nanoindentation	18.07
	Endplate – Sagittal	Nanoindentation	18.0
	Cortical Shell – Transverse	Nanoindentation	18.0
	Axial Trabeculae – Longitudinal	Nanoindentation	22.72
	Radial Trabeculae – Longitudinal	Nanoindentation	16.3
	Circumfrential Trabeculae	Nanoindentation	15.7

Table 4: Elastic modulus of bone specimens and the method by which they were determined. '*' indicates information summarized by Bayraktar [23].

Reference	Region	Yeild Strain (%)	Ultimate Strain (%)
*Lindhal[35]	Vertebrae	6.1 (Comp)	9.0 (Comp)
	Tibia	6.9 (Comp)	11.6 (Comp)
*Mosekilde[36]	Vertebrae		7.4 (Comp)
*Hansson[32]	Vertebrae	6.0 (Comp)	7.4 (Comp)
*Turner[38]	Bovine Distal Femur	1.24 (Comp)	
Kopperdahl[31]		.81 (Comp)	1.45 (Comp)
	Vertebrae	.78	1.59
*Rohl[37]	Proximal tibia		1.55 (Ten)
*Keaveny[34]	Bovine Proximal Tibia	.78 (Ten)	1.37 (Ten)

Table 5: Elastic/ultimate yield values of bone from various specimens. '*' indicates information summarized by Kopperdahl [31].

Chapter V - Subsidence and Vertebral Body Modeling

Subsidence is a failure mechanism that can occur after implantation of a device, it is notable in cases of vertebral body fusions. It is defined as the loss of postoperative intervertebral disc height and has been shown to occur in as many as 77% of patients after fusion surgeries [50]. According to actuarial rates subsidence occurs at 63.4 and 70.7 percent at 12 and 16 weeks, respectively [50]. Occurrences of subsidence are thought to be due to failure of the cortical bone of the endplate, which may be attributed to compressive stresses, or a failure of the implanted device specifically bone graft material [69].

Significant subsidence has been defined differently for the lumbar and cervical regions of the spine. Losses of disc height of 2 mm in the lumbar spine and 3mm in the cervical spine have been considered relevant benchmarks [50,70,71]. Another indication of subsidence is the change in lordic curve of the cervical spine. Changes in angle between the endplates, at the surgical level in the case of fusion, would indicate that the device is migrating into the vertebral bodies. Angle changes have been measured at a lordic increase of 1.6 degrees postoperatively to a follow up lordic decrease of 2.5 degrees [71]. The reduction in angle indicates that either the anterior or posterior part of the implanted device had subsided into the vertebral body. This failure is also a localized failure that is initiated by high contact forces generated by implanted disc devices.

Understanding the endplate morphology and biomechanics is crucial to the future success of implanted devices and finite element models. Several studies have been aimed at determining the thickness, strength and density of the vertebral endplates of the cervical spine by directly measuring cadaver specimens. The thickest regions are in the posterior region of the superior endplate and the anterior region of the inferior endplate with the central region being the thinnest [53,54,55]. Mechanically the thicker regions of the endplate are stronger than thinner areas [39]. Oxland showed that the thinner, middle lumbar region had a mean failure load between approximately 60-100 N, and increased toward the endplate's thicker peripheral regions, to a load of approximately 175 N (Grant et al, 2001). Density scans of the endplate, as measured by peripheral quantitative computed tomography (pQCT) scans, reveal that the endplate bone is denser in thicker regions [40]. Results show that an increase in bone density from 150 to 375 mg/mm^3 equates to a stiffness increase from 100 to approximately 200 N/mm. These same regions, which have a greater density and are thicker, also have an increased mineral deposition than thinner regions of the cervical endplates [42,72]. The increased mineral deposits were located in areas of the endplate that typically have the highest indentation test results and therefore higher failure limits [39,42,72].

Subsidence is a global failure mode that is the result of failure of the intervertebral bone. Engineering materials fail when the load carrying capacity is exceeded. This can be an overload of stress or the strain of bone exceeding failure limits. Measuring the stress and strain of vertebral bone is difficult. Anatomical differences between specimens make a generalized method of strength measurements

very difficult. Finite element methods have been employed as a method to measure stresses and strains. The limitation of finite element analyses is that they need to be verified by experimental studies. The non-linearity of the material response also requires a large amount of computing time to converge on an answer. Not only is the material properties of bone complicated but the geometric distribution is also very complicated. Micro computed tomography (μCT) scans have the ability to view trabecular and cortical bone on scales that can incorporate wide variations of bone distributions. The drawback is that the amount of information as far as geometry and degrees of freedom is so large that computing time is increased again.

Frequently theoretical vertebral geometry is constructed from anthropometric data [73-75]. The anthropometric data is typically compiled from measurements taken on a large sample group of cadavers. Theoretical models usually assume geometric properties of parameters that are difficult to measure directly and cost effectively, for example cortical shell thickness. Experimental models built from CT's also have material property limitations but are well suited for replicating anthropometric geometry for a single user. In both cases some assumptions need to be made concerning shell thicknesses. Several studies simplify the cortical shell and endplates as a shell with constant or only a slight variation in the endplate. The goal of this study is to determine the adequacy of a half millimeter endplate approximation.

A 3-dimensional linear elastic model of the C3 vertebrae was constructed from CT images of a 25-year old female that consisted of the vertebrae's bony structure. MIMICs 13.0 (Materialise, Ann Arbor, Michigan, USA) was used to convert the CT images

to a 3-D model. The 3D model was smoothed and meshed using 3-Matic (Materialise, Ann Arbor, Michigan, USA). From 3-Matic an orphan mesh was imported into Abaqus 6.9 (Simula, Providence, Rhode Island, USA) for post-processing. This experiment considers the thickness of the superior vertebral endplate. The superior endplate was modeled in four different ways, labeled Model 1 through Model 4. The first model, Model 1, used a half-millimeter thick approximation for the superior endplate. Model 2 assumes the endplate has been completely removed. The removal was modeled by the actual removal of the shell elements exposing the volume elements of the core. Model 3 had a superior endplate that is divided into three regions [55]. Model 4 had a superior endplate divided into seven regions [74]. Cancellous core and endplate stress and strain values were be collected and compared. The thickness and region distributions are presented in figure 7.

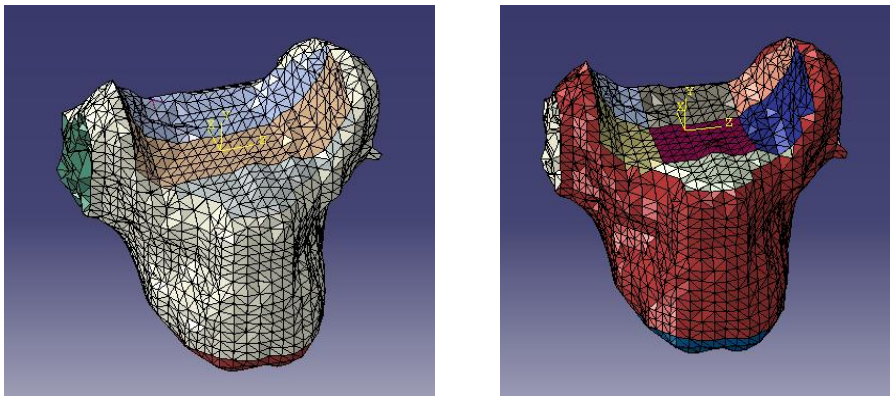

.796 mils		
.502 mils		
.524 mils		

1.115	1.09	1.093
1.066	.742	1.063
	.841	

Figure 7: Finite element models of the vertebral body with the posterior elements removed. The numbers listed below are the modeled thicknesses of the vertebral endplate. The colored regions of the vertebral models correspond to the colored numbered regions.

The finite element model was constructed with 60697 tetrahedral elements and 13651 nodes. The cortical shell was created with 4552 offset shell elements, less for the model with the removed endplate. The shells of the inferior endplate and the radial cortical shell were set to a half-millimeter thickness. All cortical bone was modeled using offset shell elements. Figure 7 shows how the endplates were sectioned. The cartilaginous endplate was not considered in this analysis because it is often removed during surgery and does not contribute significantly to the stiffness of the endplates [75].

Assigned material properties have been previously well documented in literature and are presented in the following table.

	Modulus of Elasticity (MPa)	Poisson's Ratio
Cortical Shell[77]	10,000	.3
Cancellous Core[76]	Ezz = 344, G1,2 = 63	.11
	Eyy = 144, G1,3 = 53	.17
	Exx = 100, G2,3 = 45	.23
Superior Endplate[74,75]	1,000	.3
Inferior Endplate[74,75]	1,000	.3
Posterior Elements[74,75]	3,500	.25

Table 6: List of material properties used for the models.

Material properties were considered to be homogenous. This is not physiologically accurate. The assumption was made that on the macro level the irregularities would be evenly distributed throughout the material sections and represented by the assigned values. The properties were made continuous from point to point and assigned in a hierarchical structure, which separates different bone categories, i.e. cortical and cancellous, into different material groups. This is clinically relevant since the material property definitions simulate bone's various material distributions and can be adapted to replicate disease or injury. The entire vertebra was broken down into posterior elements, cancellous core, radial cortical shell and the superior and inferior endplates. The cancellous core of the vertebral body was assumed to be anisotropic. The axial direction is the strongest due to the difference in cortical bone structure and alignment in the axial direction along lines of stress [6,7].

The models were statically loaded with an axial force of 1000 N and flexion and extension moment of 7.5 Nmm. To avoid the concentration of stress from point loads a pressure distribution was applied to the superior endplate. In this scenario, a higher

stress peak develops in the same direction as an applied moment. For example a flexion moment would have a resultant distributed load with a compressive stress peak in the anterior region of the vertebral body. The boundary conditions consisted of fixing the inferior endplate in translation and rotation.

The results show that the endplate stresses are all approximately the same in magnitude and location. The values of stress calculated in this analytical model are presented in the following table and figure.

	Endplate Flexion (MPa)	Endplate Extension (MPa)	Percent Diff, Model 1 vs. Model 3,4	Core Stress Flexion (MPa)	Core Stress Extension (MPa)
Model 1	24.6	25.6	N/A	17.1	34.5
Model 2	N/A	N/A	N/A	74.8	38.2
Model 3	20.7	15.7	17.2,47.8	13.1	8.5
Model 4	19.5	19.5	22.5,26.9	20.5	30.14

Table 7: Stress results from the finite element analysis. The maximum values from the core and the endplates are reported for each loading condition. The percent differences for the endplate values were calculated. Model 2 consisted of a removed endplate therefore the lack of N/A values in the endplate results.

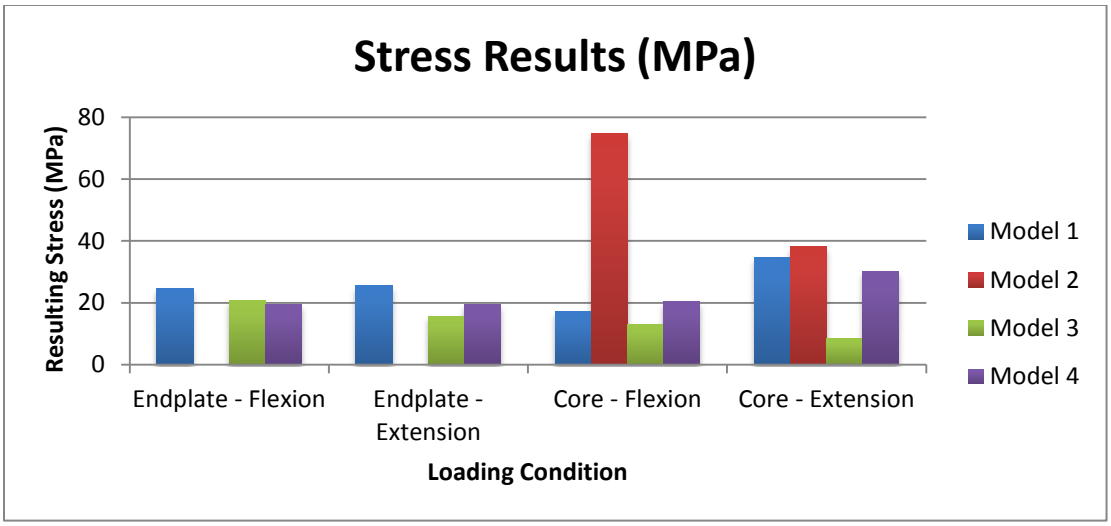

Table 8: Plot of the stresses form each model. The endplates experienced similar results. The core showed the highest stress in flexion without an endplate.

The von Mises stresses range from a minimum of 15.7 MPa, Model 3 in extension, to a maximum of 25.6 MPa, Model 1 in extension. The endplate stresses are also well under the failure stress for cortical bone. The cancellous core stresses are less consistent. A stress range of 8.5 MPa, Model 3 in extension, to 34.5 MPa, Model 1 in extension, was recorded in cases with endplates present. These values are greater than that of the listed failure stress for cancellous bone of 4 MPa. In the models with the removed endplate, core stresses reach a maximum of 74.8 MPa, which is much greater than the 4 MPa failure limit.

The strain analysis shows similar results. The half millimeter model has approximately the same strain as the more detailed endplate thickness models. Once again it is seen that the removal of the endplate increases the overstrained elements as a percentage of the entire volume of the vertebrae. The maximum percentage of post-yield strained bone was under tension in the extension models. Only one vertebra was examined so this cannot be said to be significant. However it does show that the

vertebral model with the simplified half millimeter endplate is an adequate approximation. The values of the strain are reported in the following table.

Model	Percentage of Vertebral Bone in Post-Yield Strain Region			
	Max Principle Strain (Tension)		Min Principle Strain (Comp)	
	Flex	Ext	Flex	Ext
1	2.16	3.50	2.94	2.77
2	3.22	5.48	5.41	5.08
3	1.40	2.61	2.11	1.88
4	2.07	3.47	3.10	3.36

Table 9: The percentage of the vertebral bone exceeding yield strain in both compression and tension.

This study shows that a half-millimeter endplate approximation can be used to adequately represent the cortical endplate experimentally. When compared to morphologically complex models the resulting half-millimeter endplate stress was 25.6 MPa and core stresses were 34.5 MPa similar to stresses in other research. It was found that the vertebral body can be modeled analytically without experimentation and can use simplified modeling parameters to save time and cost. Investigational tools and computational methods are constantly improving. Simplified models however can be used to make a quick estimate of the vertebral body's health and strength without the use of super-computed models. Further understanding of regional stress characteristics will be valuable for the design of implantable devices.

The knowledge of stress and strain peaks indicates regions of increased stress. These regions would be more prone to fracture due to porosity distributions. The pores provide stress raising conditions that would cause fracture at gross stress levels below the yield stress of the deterministic material properties. The finite element model above is slightly different than the fracture analysis that will follow. The primary difference is that elements of cortical bone of the vertebral body are modeled as shell elements. The

fracture following fracture analysis considers the fracture associated with the bending of a beam. The stresses in the beam require depth and a load perpendicular to the axis of the beam to generate stress while the shell elements would generate stress by being stretched in plane.

While the mechanics of the element being stressed are due to different mechanisms the areas of the vertebrae that are stressed should be similar. The following analysis will develop probabilistic criteria for estimating the risk of fracture at a certain position under a specific loading condition.

Chapter VI - Bone Fracture Mechanics

The size of pores in cortical bone is important because the presence of voids changes the mechanics of the cortical bone. The presence of a crack will cause a material to fail before it reaches its yield strength. The distribution and geometry of the crack determines when and where a failure may begin. Typically cracks do not open in regions of compression; here they have a tendency to close. In tension regions the crack will open. The crack opening resistance is a function of the specimen's geometry, material properties, orientation with respect to loading and the crack's geometry.

The ability of a material to resist crack formation can be described by its toughness K. Due to the porous structure of bone as described above the mechanical characteristics of bone cannot be solely described with critical stresses and strains, hence the necessity to understand the stress intensity caused by cracks in bone. Considered in this report is the linear-elastic fracture mechanics (LEFM). The LEFM theory dictates that there is small-scale yield or no yielding before fracture. If the LEFM theory is to be applied, the plastic zone at the crack tip must be sufficiently small. The radius of the plastic zone can be checked with the yield stress of the material being investigated and the stress intensity factor. A radius of 2r (2x the radius) ahead of the crack tip is acceptable limit [5].

Cracks can occur in three different modes. Mode I is a tensile failure, Mode II is a shear failure, and Mode III is a tearing failure. Mode II is a crack forming parallel to the

plane of the crack and perpendicular to the crack front. Mode III is crack parallel to the plane of the crack and the crack front.

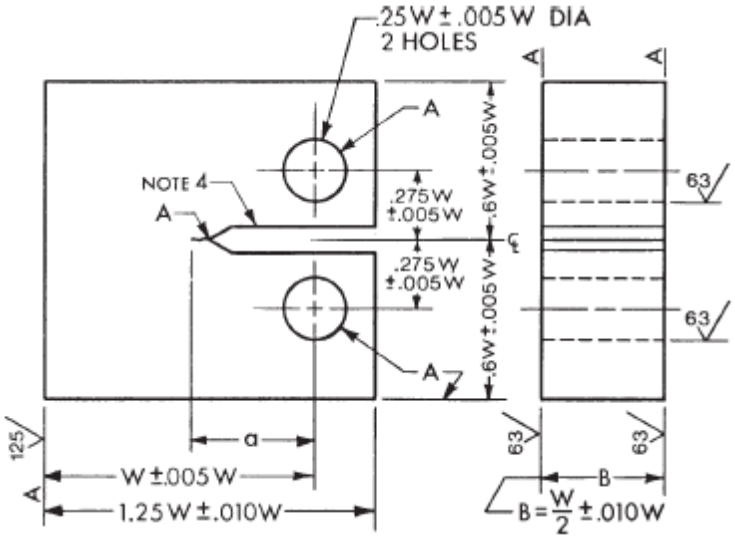

Figure 8: Mode I fracture opening in compact tension specimen ASTM E-399 [78].

Mode I, which is a tensile failure, will be the only mode investigated in this analysis. The tensile failure can be generated in several ways. One would be if a block of material were being pulled apart at the base parallel to a wide face of the material. Due to the high nature of variability of physiologic loading and anisotropy of bone there is a combination of failure modes possible in the cortical bone of a vertebral body. However tensile strength of a material is an important material property. The reduction of the tensile yield becomes increasingly important.

Several investigations study the cracking of cortical bone using human and bovine femurs. The femur is used extensively because of the size of the bone and its ability to conform to ASTM size standards [78]. According to ASTM E-399 the width of the specimen and the crack length must exceed a value of $2.5(KI_c/\sigma_{ys})^2$. If the values of the thickness of the specimen and the crack length do not exceed these values then

plane stress with poisson's effect must be considered. If the values are above the limit then plane stress is the only necessary consideration. According to ASTM E-399 the ratio of the crack length to the thickness should fall in the ratio of 0.45 to 0.55. The ratio of the distance between the thickness and the load application to the thickness of the specimen should equal 2. For bending a W/B ratio in the range of 1 to 4 may be used. The dimensions of the femur lend itself nicely to the ability to make specimen samples that fall within the required specimens.

As previously stated the stress intensity factor is partly a function of geometry. The geometry or shape function includes the geometry of the crack and the geometry of the specimen, hence the requirements of ASTM E-399. The requirements on the crack dimensions pertain to the cracks aspect ratio; the ratio of the height to the width. The crack half-width a (half the long diameter) must be larger than the half-height (half the short diameter of the crack). This lends itself well to the geometry of randomly distributed porosity which can be considered more elliptical than circular. Cement lines between osteons form sharp points as well. The important dimension is the half-width value 'a'. This value becomes the descriptor for the length of the crack. An important crack length is the length below which elastic yield mechanics hold and above which brittle fracture determines strength. This is the crack transition length for a material.

Another important geometry trend is that of the specimen in relation to the crack. This geometry locates the crack within the specimen. Because bone is a non-homogenous structure that acts like a fiber-reinforced structure there have been studies to find shape functions for bone [15].

A commonly used equation for the fracture toughness of bone was established by Behiri and Bonfield [14,18] and has been used extensively since. That equation is as follows:

$$K_{Ic} = \frac{P_q Y}{(BB_n)^{1/2} W^{1/2}} \quad \text{(Eqn. 2)}$$

Where: K_{Ic} = The fracture toughness of the specimen

P_q = The moment applied at the point of interest

Y = Shape function

B = Thickness of the specimen

B_n = Reduced thickness of the specimen at the placement of the crack

W = The distance from point of load application to the opposite end of the specimen

This equation is modification of the more recognizable equation for fracture:

$$K = FS_g\sqrt{\pi a} \quad \text{(Eqn. 3)}$$

Where: K = stress intensity

F = shape function

S_g = stress applied to specimen

a = crack length

In this case Y is comparable to $F\sqrt{\pi a}$ and S_g is comparable to $\frac{P_q}{(BB_n)^{1/2}W^{1/2}}$.

In this equation P_q is a critical loading point in which the crack propagates and energy is lost to create a fracture. B is the thickness of the material and B_n is a possible a reduction of material thickness to guide the crack parallel to the crack. W is the length from the bottom of the specimen to the point of load application. Y in the equation is

the shape factor of the specimen. Several studies have used quite varied forms of this shape function. Typically it is a higher order polynomial in terms of the initial crack length a_o and the previously mentioned W.

The following shape functions have been used to determine the crack intensity value.

$$Y = \frac{3\alpha^{1/2}[1.99 - \alpha(1-\alpha)*(2.15 - 3.93\alpha + 2.7\alpha^{2)}]}{2(1+2\alpha)*(1-\alpha)^{1/2}} \quad \text{(Eqn. 4)}$$

$$Y = \frac{(2+\frac{a}{W})}{(1-\frac{a}{W})^{3/2}}\{.866 + 4.64(\frac{a}{W}) - 13.36(\frac{a}{W})^2 + 14.72(\frac{a}{W})^3 - 5.6(\frac{a}{W})^4\}$$

(Eqn. 5)

$$Y = 29.6(\frac{a}{W})^{1/2} - 185.5(\frac{a}{W})^{3/2} + 655.7(\frac{a}{W})^{5/2} - 1017(\frac{a}{W})^{7/2} + 638.9(\frac{a}{W})^{9/2}$$

(Eqn. 6)

Where: a = crack length

W = thickness of beam/specimen

α = a/W

The ASTM E399 A3.2 (Eqn. 4) is used for a three-point beam bending test. The test specimen of the beam-bending test must also conform to very specific dimensions as well. Also included is a multiplier for the length of the unsupported length of the beam. ASTM E-399 controls the beam specimen dimensions. One of the requirements of the beam-bending ASTM standard is the presence of a single preformed crack.

To determine if the material strength has been limited by a crack, the stress intensity developed by an initial crack size (K_I) must be compared to the governing

fracture toughness factor (K_{Ic}). K_I is the result of the previously formulated equation. P_q is the limit of the elastic region of the stress-strain curve. P_q can be assumed to be the stress limit that applies to the fracture stress in linear elastic fracture mechanics and the shape function reduces the failure stress at the point. The stress intensity factor is limited from being a direct measure of P_q via the shape function F or in the case of bone Y.

The load can be considered in terms of stress applied to the specimen with a crack. In instances of point loads the stress can be determined by dividing the load by the cross-section parallel to the crack direction. In cases of an applied moment the stress can be calculated dividing the moment by the elastic section modulus of the specimen. It is important to examine the crack in the tension region generated by the moment. Since the effects of the crack length have already been addressed in the shape function it is applicable to use the bulk specimen cross-section and not using the net section that would take into account the crack area. Based on the critical crack length at a specific loading it may be possible to find the critical crack length.

As the crack opens up there is a release of strain energy associated with the crack opening. The energy stored in the crack can be measured in similar ways to a linear elastic spring. The energy applied to the crack can be found from the area under the load deflection curve. As the crack opens up the area under the curve is reduced. The change in the energy dU is the reduction in the area of the curve multiplied by the thickness of the material. The value G can be considered as the energy per crack area to extend the crack [5].

Femur studies have taken several anatomical features of bone specifically cracks in the transverse or longitudinal direction. The femur lends itself well to study this as the osteonal structures tend to run along the long axis of the bone [57]. This structure makes it easier to identify the proper direction of testing in the transverse or longitudinal direction. Also the size of the femur allows samples to be collected that better conform to the ASTM E399 requirements.

Various finding of K_c and G_c for bone has been found from different orientations and sizing conditions. Also several comparisons have been made between bovine and human bone. Table 10 shows researched values with emphasis on Mode I failures.

Study	Direction	Thickness	K_c	G_c	Source
Yan[16]	Transverse	4	5.1 ± 0.5	-	Bovine
	Longitudinal	4	2.6 ± 0.3	-	Bovine
Norman[17]	Longitudinal	2-9	4.68 ± 6.73	240 – 988	Bovine
	Longitudinal	7	4.76 ± 1.09	596 ± 134	Bovine
	Longitudinal	2	4.69 ± .65	661 ± 220	Human
	Longitudinal	3	4.48 ± .89	579 ± 308	Human
Wright/ Hayes[83]	Longitudinal	1.85 – 3.8	3.04 – 3.85	819 – 1524	Bovine
Bonfield[81]	Longitudinal	2	2.4 - 5.2	920 – 2780	Bovine
Behiri/Bonfield[13]	Longitudinal	2	4.46 – 5.38	1726 – 2780	Bovine
Behiri/Bonfield[80]	Longitudinal	1.5	2.1 - 4.7	-	Human
Behiri/Bonfield[14]	Longitudinal	.5 – 2.0	2.8 – 6.3	630 – 2884	Bovine
Behiri/Bonfield[12]	Longitudinal	1	3.2	-	Bovine
	Transverse	1	6.5	-	Bovine
Norman[82]	Longitudinal	3	6.67	1191	Bovine
Feng[18]	Longitudinal	5	3.0 ± .24	644 ± 102	Bovine
	Transverse	5	6.0 ± .41	1374 ± 183	Bovine

Table 10: Summary of Fracture toughness limits Kc and strain energy release rates Gc of and the thicknesses used for the biomechanical testing of the specimens.

From the chart above a variation of K_c can be found when compared to the thickness of the specimen and ratios of a/W. Bonfeild [13] showed a constant K_c with an

a/W ratio less than 0.7. The criterion of K_c has been shown adequate for the onset of fracture in haversian bone [17]. The LEFM method predicts the stresses in the vicinity of the crack tip and not at the crack tip itself. The crack tip itself behaves in a way similar to that of polymers [17].

It must also be noted that forces act in several different ways due to loading conditions and the anisotropy of cortical bone. Mode I fracture toughness, tensile, is below that of Mode II and Mode III, shear and tear [18]. This behavior is consistent with that of fiber reinforced materials.

To the author's knowledge cervical vertebral cortical bone has not been investigated for fracture in this manner. Typical investigations include the correlation to the incidence of failure compared to some other extrinsic property like bone mineral density or cancellous architecture (24,33,47). While these investigations are important to understand the likelihood of failure is not understood intrinsically.

Chapter VII – Probibalistic Framework for Evaluation of Toughness of Vertebral Cortical Bone

The cortical endplate of the vertebral body was modeled as a beam in a closed form model. Physiologically the load sharing between the trabecular core and the endplate is complex. When a healthy disc is present the endplate is under tensile stresses. When the disc is replaced the forces transferred cause a compressive stress in the endplate. While this is the case there are still some regions of tension within the endplate region [45]. The change in the load upon implantation of the device is still a complex situation. Beam mechanics do not directly reflect what the physiologic response is to loading, however, can be used as an analysis method do determine the strength of the endplate. This method may be useful in verifying biomechanical testing.

The model begins with assigning a beam length. The length along the beam is considered as a percentage of the length to make the calculations easy to replicate and change for a variety of uses. The next important aspect is the cross sectional area of the beam. Considered here were the measurements taken from several studies [47,53,54, 55]. These measurements of the cervical endplate were used to develop a thickness function. Mid-Sagittal thicknesses were taken. This then sets up a bending scenario in which the beam is oriented in the antero-posterior direction. That being said many different beams could be constructed in many different directions in terms of axial

alignment. A purely coronal beam could be modeled or a purely sagittal beam could be modeled.

Thickness data was collected along the mid-sagittal plane of the cervical vertebrae. The data was collected as a function of percentage around the central region of the vertebrae. For example the center measurement was 0 and in the left and right direction plus/minus 20% and 40 % of the vertebral body was measured for thickness. The following thickness data was used to create an equation of thickness across the endplate in terms of the half percentage from the center of the endplate.

Mid – Sagittal Vertebral Endplate Thicknesses (mm)											
	Pitzen		**Edwards**		**Hulme**		**Panjabi**		**Inf**	**Sup**	**Tot**
%	**Inf**	**Sup**	**Inf**	**Sup**	**Inf**	**Sup**	**Inf**	**Sup**	**Ave**	**Ave**	**Ave**
-40	1.025	1.198	0.468	0.39	0.85	0.95	-	-	0.781	0.846	**0.813**
-25	-	-	-	-	-	-	0.558	0.796	0.558	0.796	**0.677**
-20	.85	.9825	0.35	0.374	0.5	0.6	-	-	0.567	0.652	**0.609**
0	.6825	.715	0.374	0.392	0.37	0.42	0.594	0.502	0.505	0.507	**0.506**
20	.9425	.815	0.362	0.38	0.38	0.41	-	-	0.562	0.535	**0.548**
25	-	-	-	-	-	-	0.698	0.524	0.698	0.524	**0.611**
40	1.12	.868	0.394	0.384	0.8	0.75	-	-	0.771	0.667	**0.719**

Table 11: The values of endplate thicknesses both inferior and superior that were used to create the function for the beam thickness.

The location as a function of percentage from the midpoint was used as the domain while the average thickness data was plotted on the y-axis. When a 2nd order polynomial was fit to the curve the resulting equation for thickness in terms of length. The following equation was developed:

$$y = 0.0002x^2 - 0.0013x + 0.5234 \quad \text{(Eqn. 7)}$$

Where: x = position on beam in terms of percentage

y = resulting beam thickness

This equation provided the basis for the thickness along the length of the beam. The thickest value from the equation is on the ends and is 1.0884 mm. The thickest values lie on the ends of the beam.

From the thickness and width a modulus of elasticity is calculated. The beam is considered to be one millimeter wide. This was done for two reasons. First the width calculations and other subsequent calculations can be simplified with a multiplier of 1. Second this data can be considered as a per unit width result. Theoretically, if the beam were widened the results could be multiplied by a ratio of the widths to one. The drawback to this is that after a certain width plate mechanics would govern and that is not covered in this model. To calculate the modulus of elasticity (E) per unit length (l) of the beam the following rectangular moment of inertia calculation was used:

$$I = \frac{bh^3}{12} \quad \text{(Eqn. 8)}$$

Where: I = moment of inertia

b = base thickness

h = height

The geometry of the beam is now known. This is one of the two parts that is needed to determine the strength of the beam. The other part is the modulus of elasticity for cortical bone. Part of the beam model assumption is that no shear forces are acting on the beam, just loads perpendicular to the long axis. For this case a linear elastic modulus of elasticity was used that conforms to Hooke's law. Several values have been investigated and the typical range is between 16-20 GPa. This model uses 18.6 GPa as the modulus of elasticity (E). The modulus can be adjusted however for flexibility.

Now that the geometry and the modulus of elasticity have been established the strength of the beam can be assessed verse the load applied. This model considers two different loading conditions. Because of the radius of curvature of the endplate, perfect contact with an implanted intervertebral device may not be possible. With that in mind two scenarios described the extremes of vertebral contact. The first case simulates the placement of flat device on the surface of a curved endplate with no common curvature. In this scenario the device would only contact the endplate at two points with point loads. The constructed model considers the point loads to be evenly spaced from the ends of the beam supports. The next scenario models exact contact between an implanted device and the endplate. This was distributed as a uniformly distributed load centered on the beam that is not as wide as the beam length. These two cases represent the best-case implantation scenario of complete device to bone contact and the worst-case scenario of contact at two points.

The load applied to the beam is of equal force for both cases. It is distributed in two different conditions as previously described. The magnitude of the load at a minimum comes from the head and the contribution of the length of the neck to the level of the vertebrae under consideration. Conservatively the entire length of the neck and the weight of the head can be considered to act on the superior endplate of the C7 vertebrae. According to anthropometric measurements the weight of the head and neck is 8 percent of the total body weight of the person under consideration [79]. For a 200 pound person that head and neck segment weighs 16 pounds. In SI units the head and neck weighs 71.2 N. This is just the load from the head and neck which the spine sees

constantly in an upright position. A larger load was considered to investigate more extreme loads. 200 N was used as a benchmark. An endplate width and depth was estimated from measurements taken of the cervical spine [85]. A depth of anterior to posterior was estimated at 20 mm. If it is assumed that the entire endplate distributes load evenly then on a per unit width the 200 N load is divided by 20 mm giving 10 N/mm through the depth. Since this theoretical beam is 1 mm thick the load applied to the unit width under investigation is 10 N. For the load case 1, described previously where an implant contacts an endplate at only 2 points the load to each point is 5 N. For the load case 2 an assumed implant with a width of 15 mm was considered that sits centered on the endplate. The second case also considers the load to come into perfect contact with the endplate. The resulting load per unit length is .667 N/mm.

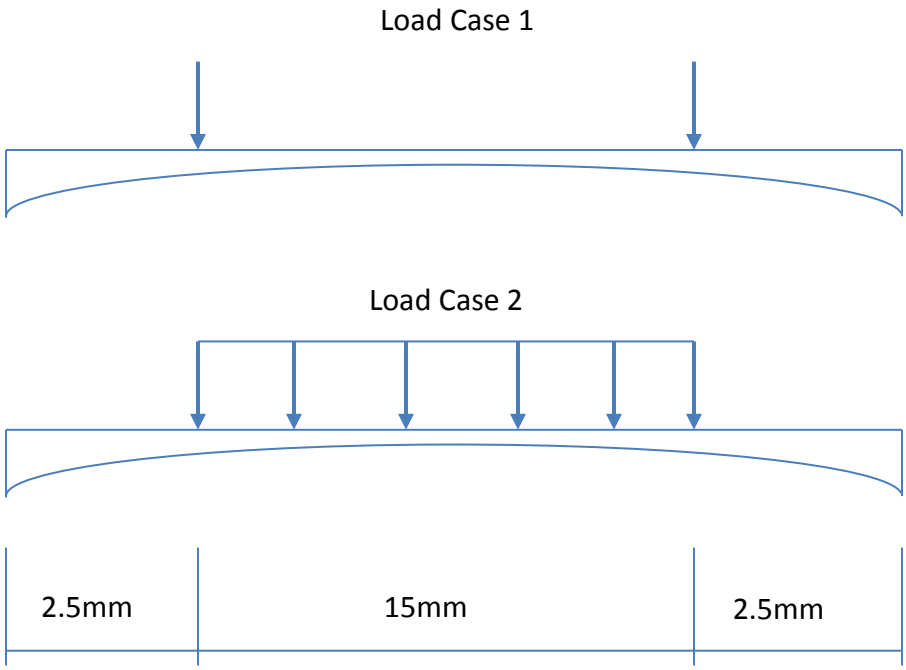

Figure 9: Diagrams of load case 1 and load case 2. Load case 1 is two equally spaced point loads. Load case 2 is incomplete uniform load.

The moment and deflection generated from applied loads were calculated using AISC design aides. For the first load case, load case 1, of two point loads simulating drastic curvature differences the design aid of two equal concentrated loads symmetrically placed was used [3] and for the second case, load case 2, of an implant where contact is continuous along the length of the implant the uniform load partially distributed design aid was used [3]. Physiologically the vertebral body shares load between the cortical shell and the trabecular core. The exact amount of load sharing is up for debate. The percentage of load that the cortical shell is responsible for has been found to be as low as 10 percent [6] to as high as 52 percent [47].

The load applied to the endplate was not reduced. If the vertebral endplate were able to be excised and tested the results would be directly comparable. The maximum bending stress in the extreme fibers can be determined the following equation:

$$\sigma = \frac{Mc}{I} \quad \text{(Eqn. 9)}$$

Where: σ = bending stress

M = applied moment

c = half height of beam

I = moment of inertia

where c is half the height of the beam at each spot on the length, M is the applied moment, and I is the moment of inertia per length of the beam with the assumption that the porosity will be normally distributed according to the investigated studies.

Now that the load per unit length and stress to the beam is known cracks are applied to the beam. To assign a crack distribution the porosity of cortical bone must be

known. Much work has been performed on cortical porosity of the femur [9-11]. Vertebral porosity is less well reported. The basis of this analysis uses femur data to construct the crack distribution along the length of the model vertebral beam.

The terms of the crack require definition. It is necessary to assume the crack is an elliptical shape with the length of the long dimension much longer than that of the short dimension. This is a requirement of crack characteristics [5]. This assumption is reasonable based on the type of pores present in the cortical bone. Based on the crack definition and placement the only variation is that of the length of the initial crack. This information is used to build the shape function, part of the stress intensity calculations. The initial crack length is an important input value for determining the stress intensity value at the crack tip. The other required information is the thickness of the specimen and the applied stress at the beam at the position of interest. The crack is considered a non-union of the cortical bone for this analysis. This means that the cortical bone may not be attached to the adjacent cortical bone. An initial diameter though is still needed to establish an initial crack length. The width of the crack is not important as long as the ratio of the length to the width is large.

The crack should also be considered a small crack. This means that at least one of the dimensions of the crack is larger than the largest part of the microstructure. Also typical of small cracks is that the specimen is considered to be an isotropic homogenous solid. This assumption was made throughout this analysis. This differs from short cracks in that the crack is smaller than the largest feature of the microstructure [4]. These types of cracks were not considered.

A Monte Carlo extension module, RiskAMP (Structured Data, New York), was used to create the crack simulation in Excel. RiskAMP is a random number generator that also has the ability to add a randomized distribution of the user's choosing to any selected cell. There are several preloaded distributions: uniform, normal, triangular, Pert, Weibull, etc. The user is prompted to enter a series on information per distribution, for example the normal distribution requires the input of a mean and standard deviation and a random set of numbers is generated conforming to the normal distribution that would fit the corresponding input criteria. The user also controls the sample size when the simulation is run. The user enters a desired sample size N when running the simulation. Once run each cell selected contains a random distribution of size N and distributed based on the criteria supplied for that cell. The reported value in the cell is the mean of the group but by no means is the only value in that cell. The value that appears in the cell can be used in later calculations of the sheet. All successive calculations are performed with the assumption that the cell value is the crack length.

The sample size of the distribution is also a user input. This model assumed that the crack placed came from a set of 500. The size of the set was important. First it was very large to maintain consistency along the length of the beam. The Monte Carlo simulator recalculates the crack distribution parameters for every crack. The large number means that the distributions are consistent in terms of mean and standard deviation. Secondly the group is set to 500 to increase the accuracy of the results. The large sample size also provides a large pool of crack lengths to be randomly generated.

The more cracks lengths that can be selected will improve the accuracy of the prediction model.

Direct measurement of the cortical porosity of the vertebral body has been difficult to find. It was assumed that the femur calculations can be applied to the vertebral body considering the nature of cortical bone. As such femur data was used to expand measurements taken in the cortical bone to expand the pool of crack modeling data. As previously described cortical bone is a denser distribution of trabecular bone. Therefore the structure should be similar to that at the femur sites. The contributing porosity factors considered in this model was the non-union pores in between osteons. The Haversian canals are closed voids inside the osteon and the fracture of this configuration was not considered. Cracks in the bone due to porosity between osteons lend itself nicely to the K_I calculations.

The porosity distribution was built from several collected porosity measurements of cortical bone sites. It was assumed that similar trends would be present in the data and ratios of certain variable were used to develop a consistent set of information to find the intraosteon porosity.

		Haversian Canals Area (μm^2)	Osteon Canals Area (μm^2)	Average Porosity Area (μm^2)	Average Measured Porosity (percentage)
Wachter[11]	Max	31244	63959	101337	26
	Min	665	26390	3100	4
	Average	4157	41621	19863	9.1
Wang[10]	Max	4717	9657	15300	-
	Min	577	22890	2689	-
	Average	2633	26362	12581	-
Fazzalari[8]	Average	13704	137210	65481	30
Bell[9]	Average	5510	55170	26329	12.1

Table 12: Data set used to develop the normal distribution of pore sizes.

All this information was collected to build the average porosity area column in the chart. The porosity area is the area between the osteons. From this column of information the minimum, average and maximum areas were calculated from the entire group and from this the radius of the modeled crack was developed.

	Average Porosity (μm^2)	Radius (μm)	Diameter (μm)
Minimum	2894	78.97	60.7
Average	19591	30.35	157.9
Maximum	58319	136.25	272.5

Table 13: Diameters used in the normal distribution for the crack sizes calculated from the average porosity data.

It was assumed that the pore size would fit into a normal. Monte Carlo has the ability to generate a truncated normal distribution which considers the minimum and maximum values as limits on the sizes that can be generated. The diameter of the crack was considered to be able to exist entirely within the beam. The sizes of the pores were deemed reasonable in that measurements of osteons and haversian canals were consistent between several studies [8-11].

Once the initial crack length is established the stress intensity factor for four models was calculated. Four models were developed according to research on stress intensity values of cortical bone and models present in texts and considering ASTM standards [5,16,17,18,19,78]. The first step was calculating a shape factor from each model for each spot along the length of the beam.

Norman [17] and Feng [18] used a shape function for the stress intensity factor developed by Behiri and Bonfield. The shape function is in terms of 'a', the initial crack length, and W the width of the specimen at that point. In this case the specimen width corresponds to the height of the beam. The shape function is applicable to the Mode I stress intensity. The equation is as follows:

$$Y = 29.6\left(\frac{a}{W}\right)^{2} - 185.5\left(\frac{a}{W}\right)^{3/2} + 655.7\left(\frac{a}{W}\right)^{5/2} - 1017\left(\frac{a}{W}\right)^{7/2} + 638.9\left(\frac{a}{W}\right)^{9/2} \quad \text{(Eqn. 6)}$$

Vashishth [19] used a shape function suggested by ASTM E-399 [78]. Again the shape function is in terms of 'a' and W and used to determine the stress intensity of Mode I cracking. The ASTM E-399 [78] shape function is as follows:

$$Y = \frac{\left(2+\frac{a}{W}\right)}{\left(1-\frac{a}{W}\right)^{3/2}}\left\{.866 + 4.64\left(\frac{a}{W}\right) - 13.36\left(\frac{a}{W}\right)^{2} + 14.72\left(\frac{a}{W}\right)^{3} - 5.6\left(\frac{a}{W}\right)^{4}\right\} \quad \text{(Eqn. 5)}$$

The fourth model by Yan [16] uses a shape function from ASTM E399 [78] and is used for a beam bending application. The function is as follows:

$$Y = \frac{3\alpha^{1/2}\left[1.99 - \alpha(1-\alpha)\left(2.15 - 3.93\alpha + 2.7\alpha^{2}\right)\right]}{2(1+2\alpha)\left(1-\alpha^{1/2}\right)} \quad \text{(Eqn. 4)}$$

Each of these shape functions and test methods has specific specimen size requirements on them according to ASTM E399 testing standards. Typically the requirement for a/W is in the range of 0.45 to 0.55. Feng [18] expanded the a/W initial condition to 0.7. Other studies have shown that an increase in the ratio of a/W (longer initial crack) increases the resulting K_c value with that associated initial condition.

Lastly a shape function from by Dowling [5] was modeled. Initially it considers a value of a/W < 0.4 can be modeled with the value 1.12 and can achieve accuracy within 10%. Another method is to use a shape function that is based on the ratio of the x position of the crack to the width of the specimen, W. This model assumes that (x position)/W is large. Near the edges this may not necessarily be the case, because the radial cortical shell that supports the endplate also has a thickness that is not considered so the assumption of the large h/b shape function was deemed most reasonable. The shape function for the Dowling model is as follows:

$$Y = \sqrt{\frac{2}{\pi a}\tan\left(\frac{\pi a}{2}\right)}\left[\frac{.923 + .199\left(1 - \sin\left(\frac{\pi a}{2}\right)\right)}{\cos\left(\frac{\pi a}{2}\right)}\right] \quad \text{(Eqn. 10)}$$

Where: Y = shape function

a = crack length

The beam has been divided into 100 slices having a corresponding width to the length of the beam over 100. A crack is assumed to be placed at each of the divisions and is assumed to be centered in the spacing. As far as the other models the main crack criteria is the a/W ratio.

The crack's assumed placement is in the tension region of the beam. The orientation of the crack is transverse to the longitudinal direction of the beam. Crack placement in the tension region of the beam to simulate a Mode I crack opening. Other modes, II and III, consider the crack to be created by shear and tearing conditions and are not considered.

From this point the calculation of the stress intensity factor of each point along the beam can be calculated. The equation for the crack intensity value was found to be the same across all studies [16,17,18,19]. Yan had a slightly different equation for the stress intensity factor. It considers not only an initial crack but also the reduction of cross section at the point the crack is initiated. If this reduced cross section is considered the same thickness as the rest of the beam the equation reduces to the same function as the other studies. The equation for calculating the stress intensity factor is:

$$K_c = \frac{PY}{B^{1/2}W^{3/2}} \quad \text{(Eqn. 11)}$$

B is the width of the beam, for the theoretical model developed B = 1 mm for the entire length. W is the depth at each point along the beam. Y is the shape function calculated according to the previously mentioned shape functions. P is the load applied to the beam at each differential specimen along the length.

ASTM E399 [78] recommends test specimen configuration that apply a tension load at two points opposite each other at one end of the specimen. The point of load application is where W is considered to start when measuring the ratio of a/W. Dowling also describes a scenario in which a specimen has tension generated by moments on each side of the specimen perpendicular to the crack orientation. This theoretical model

assumes that the load application to each compact specimen is supplied by a bending moment perpendicular to the crack orientation. The beam model is constructed slightly differently. The beam model also has restrictions on the size of the span to width of the specimen. This ratio is on the order of 4 to 5 for span to width. It was assumed that the equations would hold for the decreased specimen width.

The critical load P is then considered the applied moment at each length of the beam. The units of moment (force times length) are not the correct units for the critical stress equation so it is adjusted by multiplying it by the section modulus at each point along the beam. This adjustment provides the correct final units for the stress intensity calculations. P_q is a particular point of interest when calculating the critical stress intensity factor. The critical K_c value is that in which a crack will grow, below that cracks do not grow. To find this value deflection is plotted verse load applied [78]. The load should increase approximately linearly with an increase in deflection. As soon as the load drops or the load-deflection curve loses its non-linearity the P_q can be determined. In the first case P_q is defined when the load-deflection curve changes direction. In the second case P_q is a 0.2% offset of deflection past non-linearity. This value of P_q is used to determine the critical crack growth length. If a stress is applied to a specimen greater than this load then cracks in the specimen should grow.

After the crack intensity value K_I is determined for each beam division the applicability of linear elastic fracture mechanics, LEFM, and plane stress/plane strain conditions are checked. A check must be made on the size of the plastic region generated at the tip of the crack. If the plastic zone becomes too large (2 times the

radius of the crack at critical stresses) then LEFM are no longer applicable. The width, initial crack length and height of the beam minus the crack must be checked to see if they are sufficiently large to surround the plastic zone at the tip of the crack, 8 times the radius of the crack tip to the boundaries is deemed sufficiently large [5]. LEFM applicability can be determined with the following equations [5]:

$$a,(height - a) \geq \frac{4}{\pi}\left(\frac{K}{\sigma_0}\right)^2 \quad \text{(Eqn. 12)}$$

Where: a = crack length

K = stress intensity

σ_0 = modulus of elasticity

Plane stress and plane strain conditions also need to be checked at each point along the beam. Thickness considerations need to be checked to see how the material will fail once fractured. The equation [5]:

$$t,a,(b - a) \geq 2.5\left(\frac{K}{\sigma_0}\right)^2 \quad \text{(Eqn. 13)}$$

Where: t = beam thickness

a = crack length

b = beam thickness – crack length

K = stress intensity

σ_0 = modulus of elasticity

determines the plane stress/strain limit. Above this value and the plain strain controls the failure below and plane stress applies. If plane strain applies the modulus of

elasticity must be adjusted to take into account poisson's effects in the transverse axis [5].

Once it was established that the beam was LEFM applicable along the length and was a plane stress condition the probability of a transition crack could be determined. The limiting crack length was found using Excel's goal seek function. The equation for the stress intensity factor was written in terms of the initial crack length. The goal seek was used to iterate the value of the crack length until Ki was that of K_{Ic}. Excel directly changes the value of a thus resulting in the length of the transition crack.

A transverse value of K_{Ic} was used as the limit for the critical stress intensity value. Cross sectional cuts of vertebral bone show that the cortical bone in the endplate is transversely distributed. The cuts show Haversian canals long axis oriented in the axial plane [65]. Because of the orientation of the osteons cracks would have to grow perpendicular to the long axis of the osteon and when they grow into an osteon would wrap around the osteon thereby increasing the stress intensity value as compared to a crack that grows parallel to the osteons long axis that would open separate the osteons like a zipper.

Once the size of the transition crack length is determined a comparison is made to the distribution of cracks at the same spot along the beam developed by the Monte Carlo plug-in. A built in function in RiskAMP, SimulationInterval, can determine the probability of the occurrence of the transition crack limit given a distribution. What is particularly useful is the probability of the crack being less than that of the transition crack length. Theoretically cracks under this length would allow the strength of the

beam to be governed by classic material property and geometry considerations. Cracks with lengths longer than the transition length would indicate the strength of the modeled beam is limited by the fracture mechanics.

Each study mentioned above has determined its own or used other K_{Ic} values for a comparison of bone fracture toughness. This theoretical beam model uses these limits as a benchmark to determine whether or not the beam has grown a crack under its loading.

Chapter VIII - Results/Discussion

The probability of a crack length being below the critical length to transition a beam to fracture mechanics was determined for both, Load Case 1 and Load Case 2, and for each model developed. The probability was determined as a value out of 1. If the probability at a point equaled 1 then the load at that point would be able to sustain any crack size in that distribution, i.e. the limiting crack length was longer than any in the generated distribution.

It should be noted that the end conditions were considered pinned not fixed. A zero value for the moment created situation in which the end conditions were not applicable.

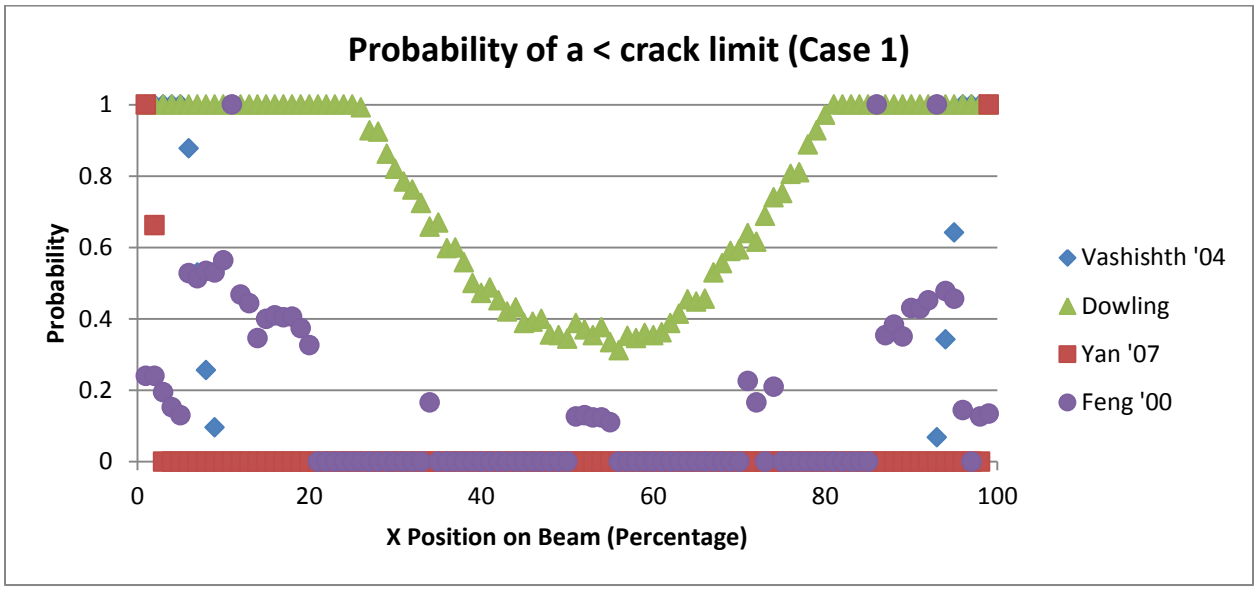

Figure 10: The Probability the present crack is less than the crack limit, load case 1.

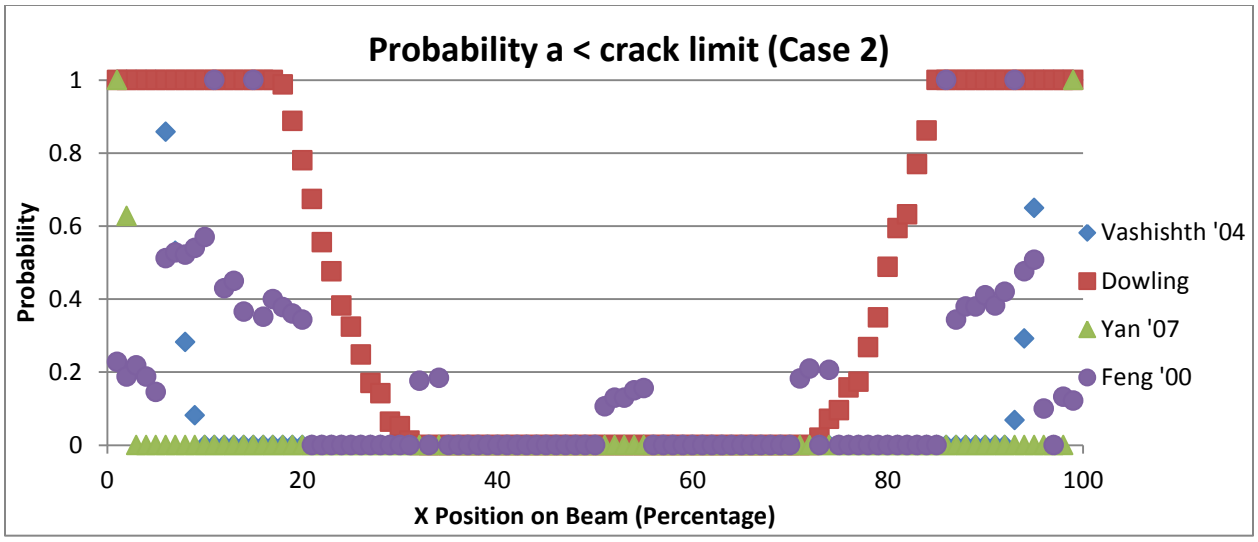

Figure 11: The Probability that the present crack is less than the crack limit length, load case 2.

From figures 10 and 11 it can be seen that the Yan beam model [16] is the most conservative model for the LEFM limits. For case 1 and case 2, 90 percent of the beam length was unable to achieve the minimum crack length. Only 10 percent of the beam had any chance of being under a limiting crack length. The span length in a 3-point bend test as defined by ASTM the span is the distance between supports. In the case of a physiologic bone sample that distance may be reduced by the contribution of the trabecular bone. While the support is not the same as in a bend test a modification to the span coefficient may yield results closer to that of the other models.

The Vashishth ’04 [19] model predicts 52% of the Case 1 and 65% of the Case 2 beams cannot meet a minimum required crack limit. This method is based on a purely compact tension model constructed on the same manner as ASTM E-399 section 4.

The Dowling model has the highest probability of a crack below the fracture limit. In Case 1 the entire beam had a chance the strength being governed by classic beam mechanics. This is most likely due to the distribution of the moment. The max

moment from Case 1 is 12.5 Nmm while the max moment for Case 2 is 31.25 Nmm. While the load is the same the moment distribution tends to increase the maximum moment as the load evenly distributes. The Dowling model also consists of a discrete moment at each section of the beam. This moment can be found directly from the bending equations. Differences in the probability can be attributed to the shape factor.

The Feng models have an entirely random distribution that seems to be more dependent on crack length than it does on the amount of stress at each point. The Feng model differs from the previous three models in this respect. The previous three models tend to be more dependent on the stress applied to the differential sections as opposed to seemingly be controlled by the crack length as with the Feng model.

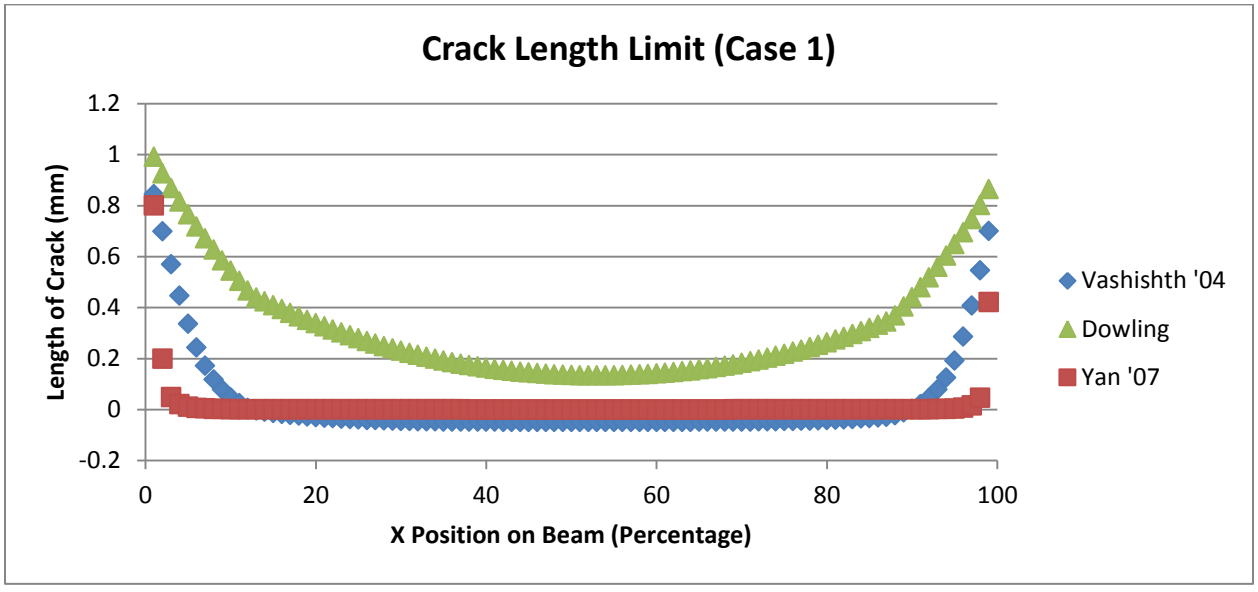

Figure 12: The calculated crack limit case per length of the beam, Feng Intentionally excluded. Load Case 1

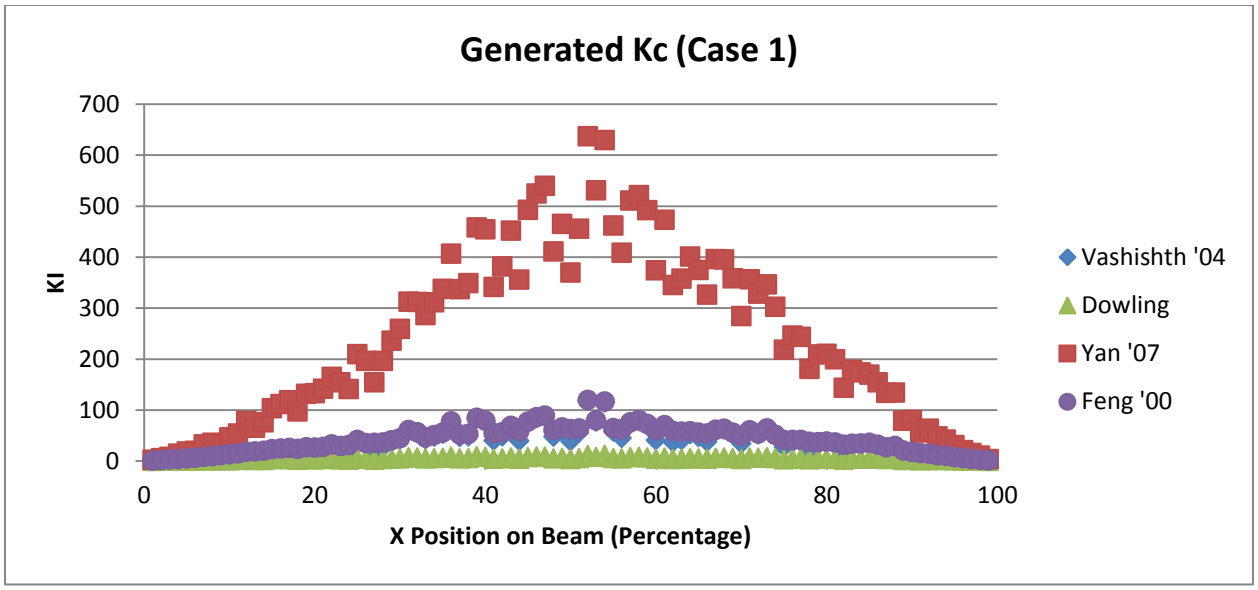

Figure 13: Stress Intensity Factor Calculated per beam length, Load Case 1

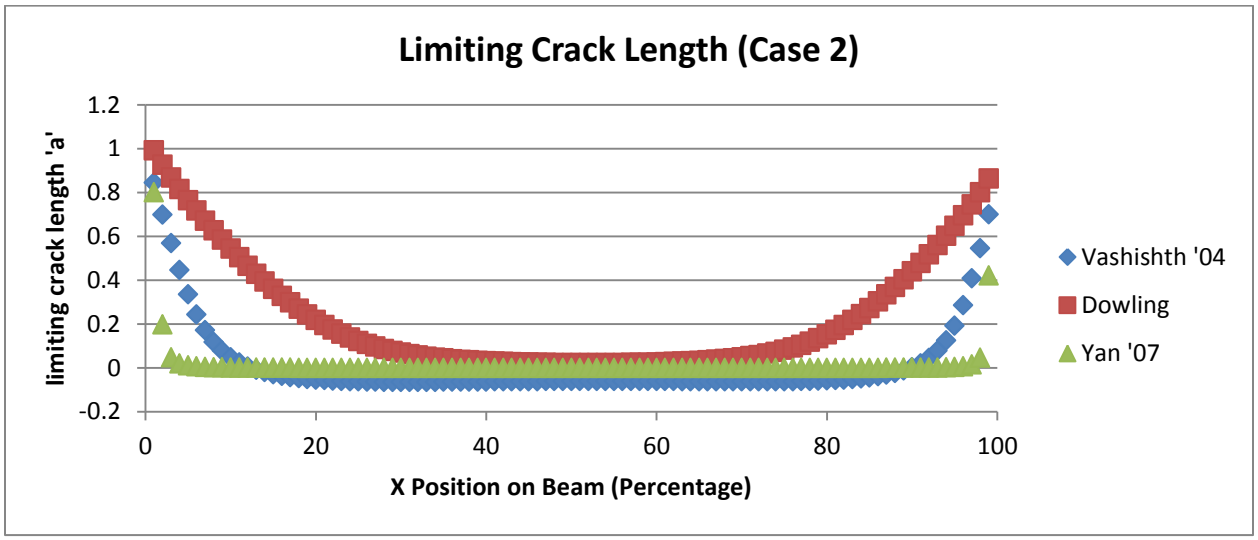

Figure 14: The calculated crack limit case per length of the beam, Feng Intentionally excluded. Load Case 2

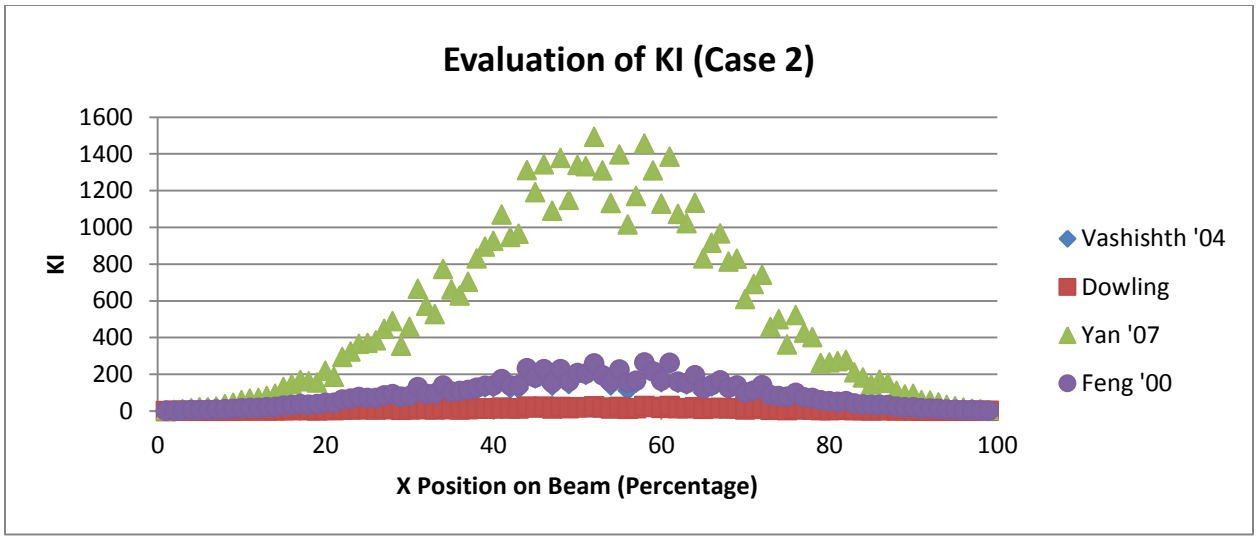

Figure 15: Stress Intensity Factor Calculated per beam length, Load Case 2

The Yan beam model [16] is the upper limit in both case 1 and case 2 for the stress intensity factor. This seems to be due in strong part to the span multiplier present in the equation for K_I. For the case of vertebral endplate tissue separated from the cancellous core, a value of 20 mm would be correct if compared to three-point beam testing. This is likely an overestimate of the stress intensity value at points along the length because the trabecular core supports the vertebral endplate at intervals closer than the 20 mm span assumed here. However if the endplate could be excised then the 20 mm span would be more appropriate leading to a higher stress intensity factor.

The stress intensity values calculated by the Vahishth and Feng models are the most similar with the Dowling model being the lower bound for the values for both load case 1 and 2. It seems that the shape function for the Dowling model may under-predict the stress intensity factor along the length. This would result in a longer than acceptable initial crack length limits.

Corresponding to the stress intensity value is the limit of the initial crack length. The limiting crack length was found by limiting the value of 'a' until the stress intensity value was below the transverse limit for bone fracture. Again the Yan beam model [16] was the least likely to have an initial crack limit below the threshold, with the exception of small distances from the supports. The Vashishth tension model [19] had a larger percentage of the beam that had crack values under the critical threshold however towards the middle of the beam the negative values indicated that in those regions any crack present would limit the strength of the bone by fracture mechanics. The Dowling model differed from the other three models and created a high end for the amount of permissible cracks. The probability was increased for cracks being beneath the threshold for the Dowling model [5]. The crack limit threshold for the Dowling model was also greater for every point along the beam than the Vashishth tension [19] and Yan beam [16] models.

The probability of a certain stress intensity value causing the crack size to exceed the threshold crack limit is a valuable piece of information. There is a limit of the stress intensity value in the transverse direction in vertebral bone but that does not necessarily mean that a crack above the crack limit threshold exists there. The probability of exceeding the threshold crack limit was calculated verse the K_I value. A Weibull cumulative distribution plot (CDF) was used to describe the probability as a function of K_I. The Weibull equation and the probability domain were graphically cut off after the point at which the crack threshold maintained 100% probability.

What this theoretical model produced was the probability of a threshold crack based on a limiting K_c of 6 $MNm^{3/2}$. The randomized values hover around the transverse K_c limit of 6. The Weibull equations for each scenario are provided in table 14. These equations fit the Weibull continuous distribution function (CDF) [4] form of:

$$f(x) = 1 - e^{-\left(\frac{x}{\delta}\right)^{\beta}} \quad \text{(Eqn. 14)}$$

Where: x = stress intensity per length K

$\delta = e^{(\text{average of probability})}$

β = 1/(standard deviation of probability)

The standard deviation and the average were calculated from the probabilities of the existence of a limit crack.

	Model	Equation
Case 1	Vashishth '04	$f(x) = 1 - e^{-\left(\frac{K_I}{2.43}\right)^{3.38}}$
Case 1	Dowling	$f(x) = 1 - e^{-\left(\frac{K_I}{1.28}\right)^{3.78}}$
Case 1	Feng '00	$f(x) = 1 - e^{-\left(\frac{K_I}{2.33}\right)^{4.25}}$
Case 1	Yan '07	$f(x) = 1 - e^{-\left(\frac{K_I}{2.67}\right)^{8.29}}$
Case 2	Vashishth '04	$f(x) = 1 - e^{-\left(\frac{K_I}{2.41}\right)^{3.26}}$
Case 2	Dowling	$f(x) = 1 - e^{-\left(\frac{K_I}{1.77}\right)^{2.20}}$
Case 2	Feng '00	$f(x) = 1 - e^{-\left(\frac{K_I}{2.31}\right)^{4.06}}$
Case 2	Yan '07	$f(x) = 1 - e^{-\left(\frac{K_I}{2.65}\right)^{6.50}}$

Table 14: Weibull distribution input parameters.

Figures 16 through 23 show the probability of crack size limit exceeding the threshold crack size that changes the strength limit to fracture mechanics. In both case 1 and case 2 the Yan beam approximation [16] and the Vashishth [19] compact tension model under-predicted the probability of a threshold crack. This can be seen by the Weibull prediction function being to the left of the distributed data. The Dowling and Feng [18] model seems to over-predict a threshold crack in case 1 and 2 because the prediction function is to the right of the data. The Vashishth, Feng and Yan models are all conservative, with respect to bone's transverse fracture toughness. The models predict cracking starts prior to reaching bone's fracture toughness limit. Due to the conservatism of the model, design considerations accounting for the probability of fracture onset, would necessarily be conservative in all cases since transverse fracture toughness is not exceeded by the model itself. The Dowling model however is different. This model shows that there is a probability that the onset of fracture will not occur when the transverse fracture toughness is met. That being said the probability of the presence of a threshold crack increases with an increase in the K_I value. Ultimately the Weibull equations can predict the onset of fracture for a sample of bone considering deterministic parameters from previously researched bone samples.

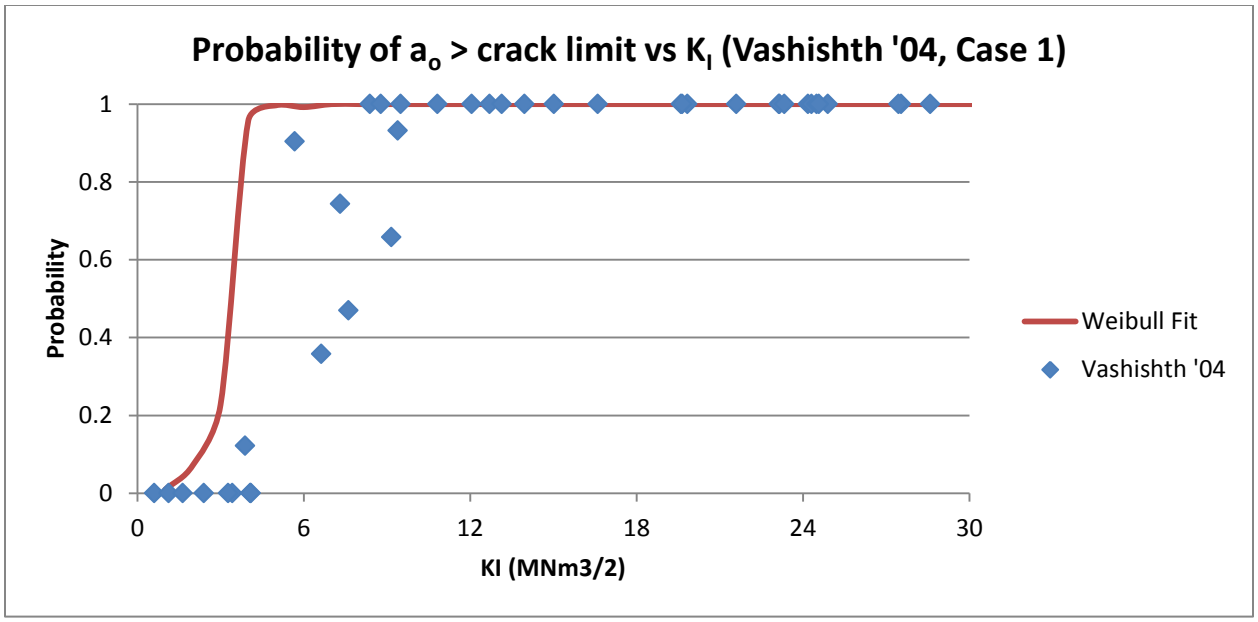

Figure 16: Weibull Probability Distribution Predicting crack length exceeding limit with respect to KI generated on beam, Vashishth Model, Load Case 1

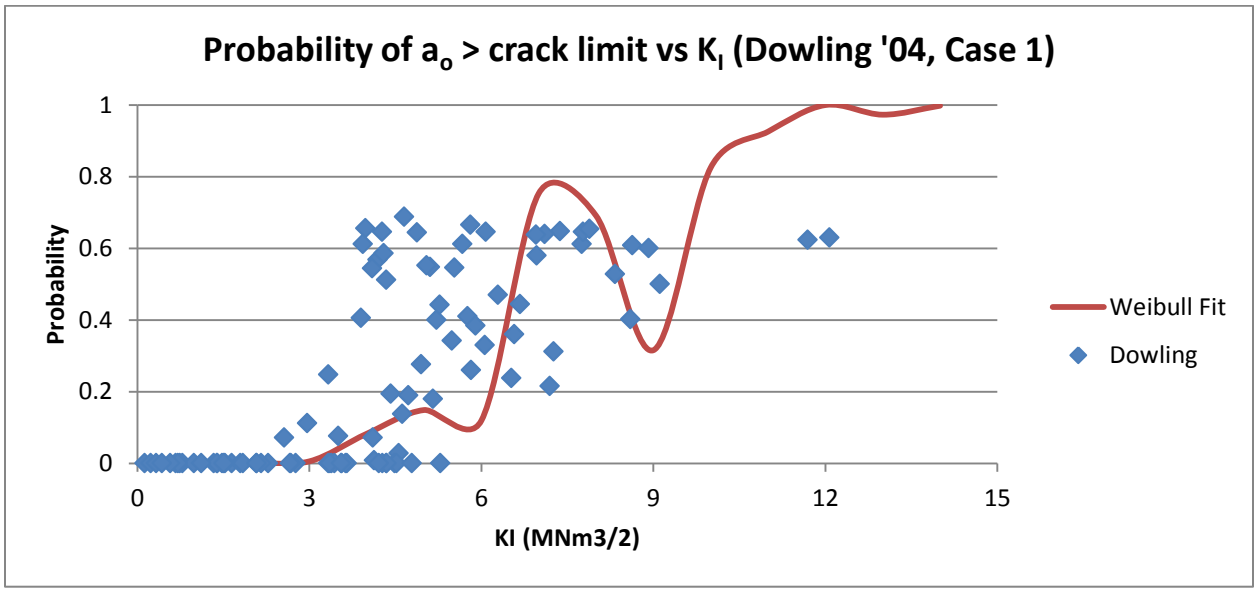

Figure 17: Weibull Probability Distribution Predicting crack length exceeding limit with respect to KI generated on beam, Dowling Model, Load Case 1

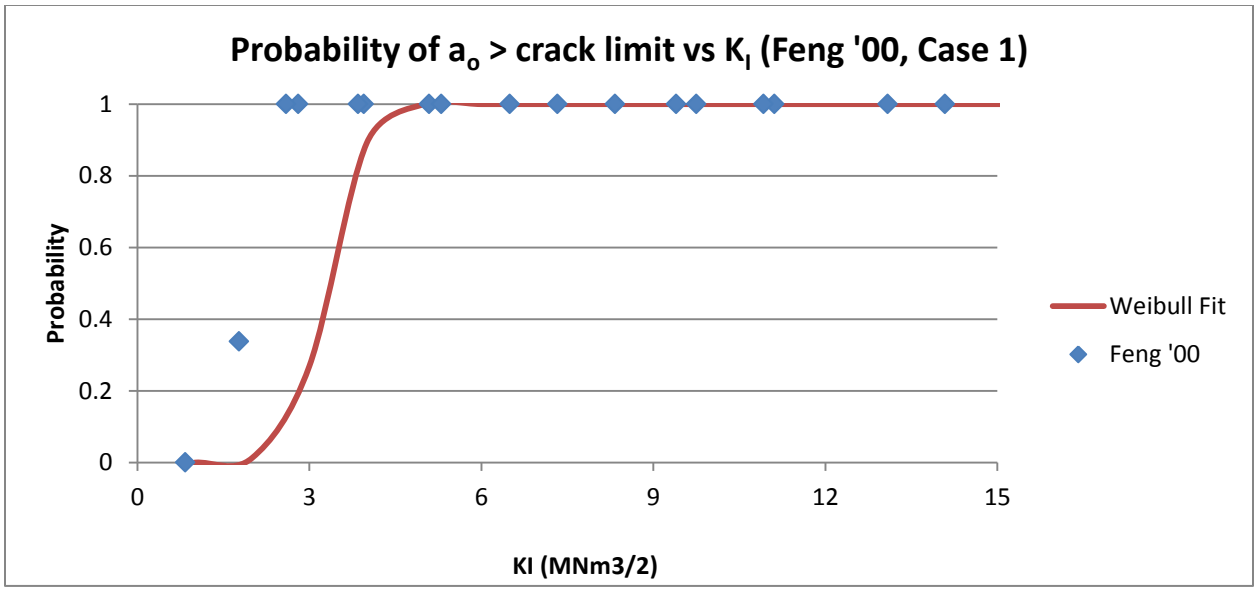

Figure 18: Weibull Probability Distribution Predicting crack length exceeding limit with respect to KI generated on beam, Feng Model, Load Case 1

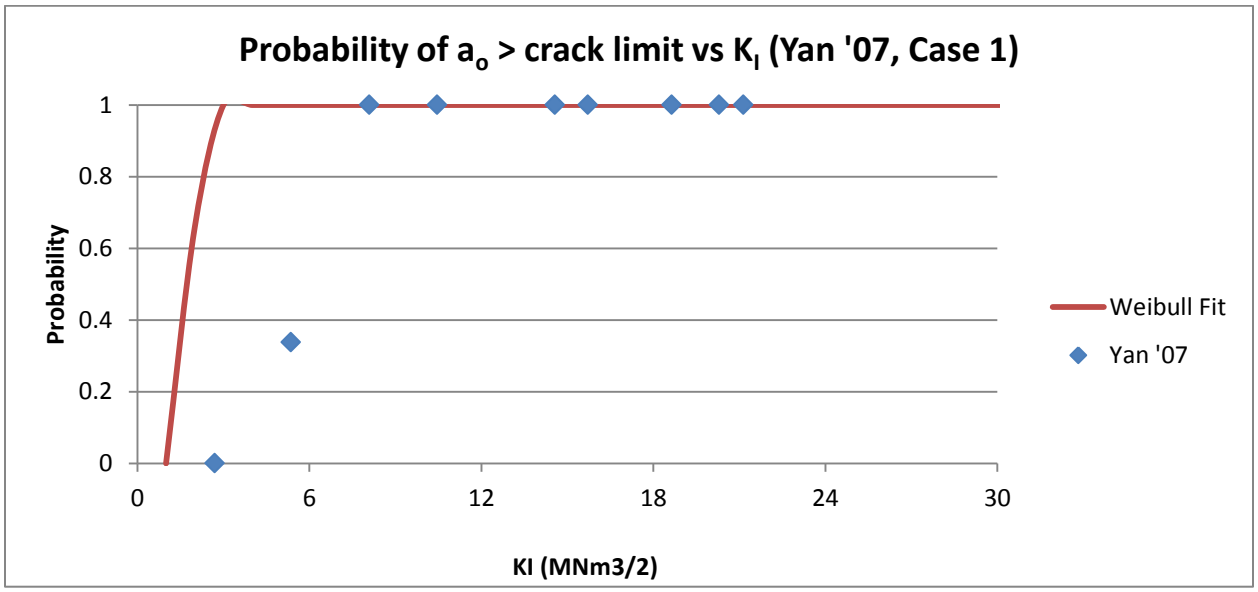

Figure 19: Weibull Probability Distribution Predicting crack length exceeding limit with respect to KI generated on beam, Yan Model, Load Case 1

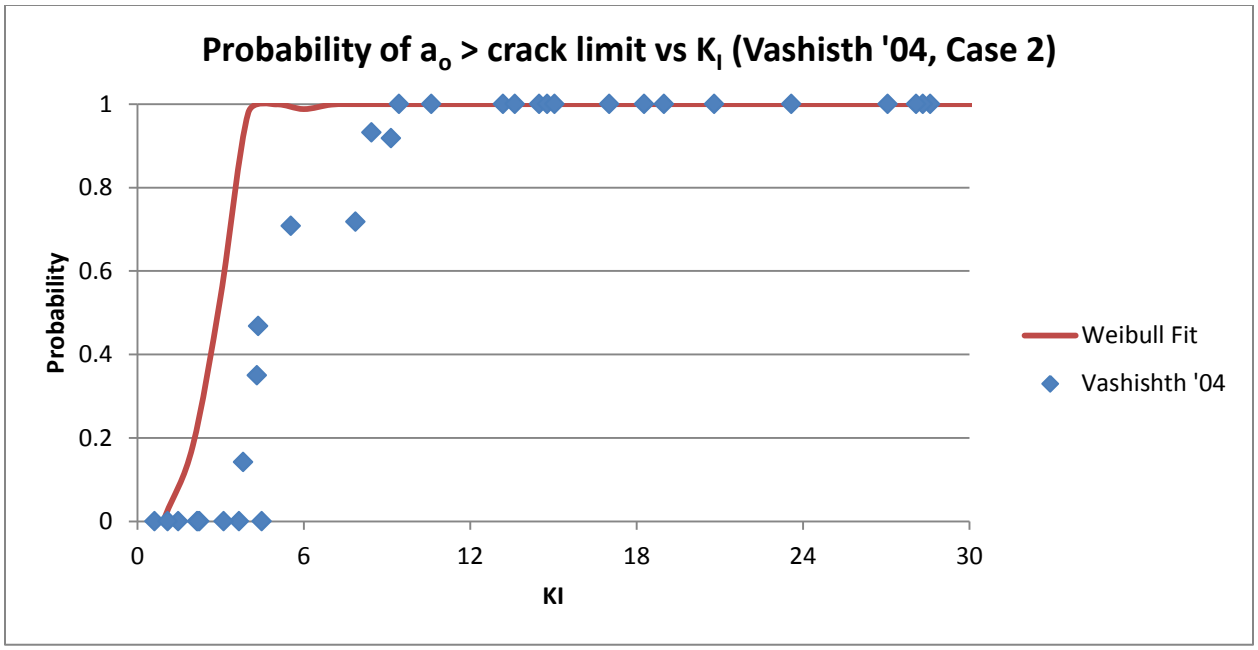

Figure 20: Weibull Probability Distribution Predicting crack length exceeding limit with respect to KI generated on beam, Vasishth Model, Load Case 2

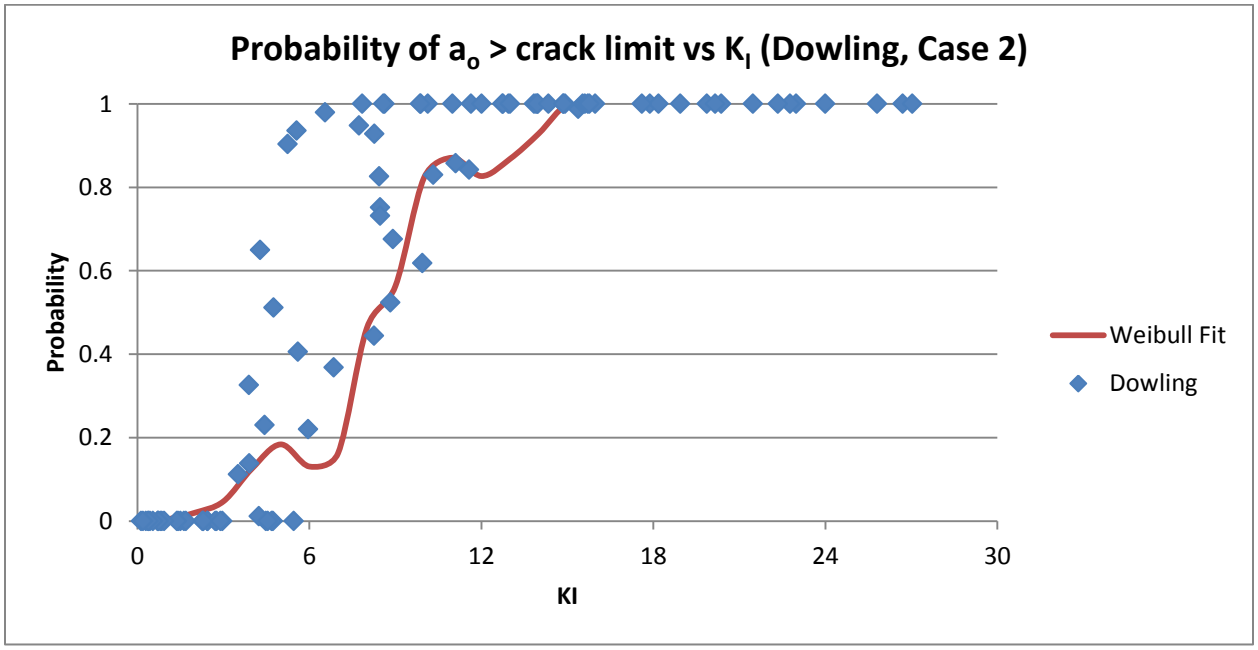

Figure 21: Weibull Probability Distribution Predicting crack length exceeding limit with respect to KI generated on beam, Dowling Model, Load Case 2

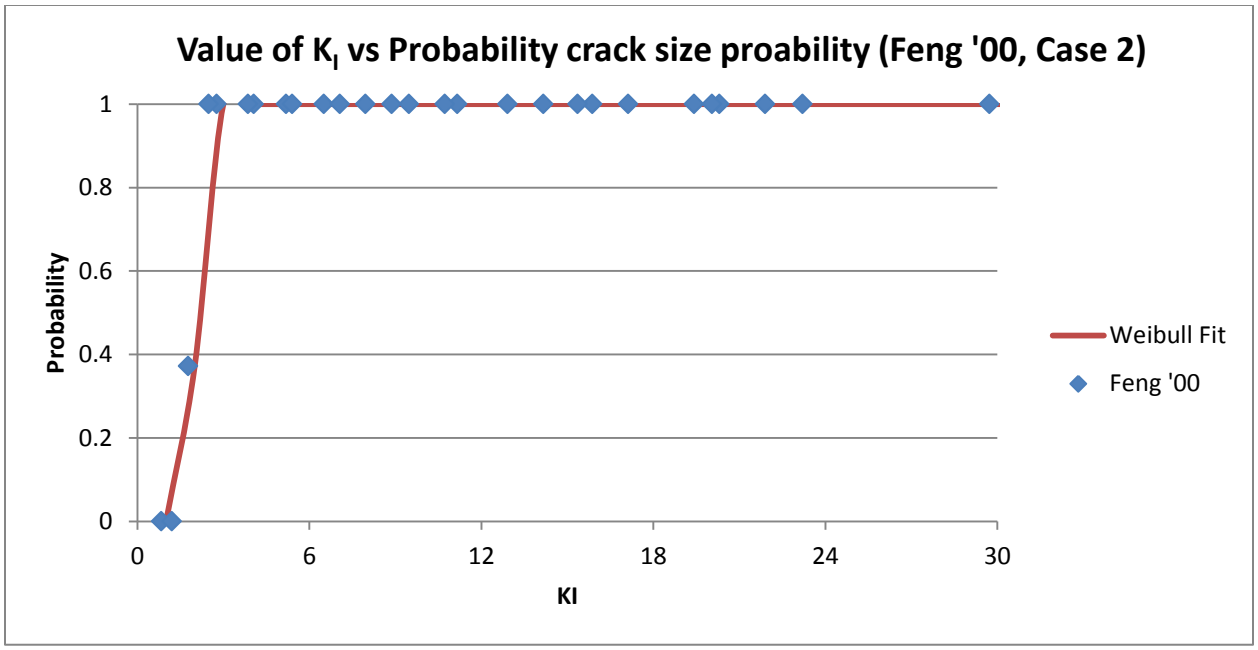

Figure 22: Weibull Probability Distribution Predicting crack length exceeding limit with respect to KI generated on beam, Feng Model, Load Case 2

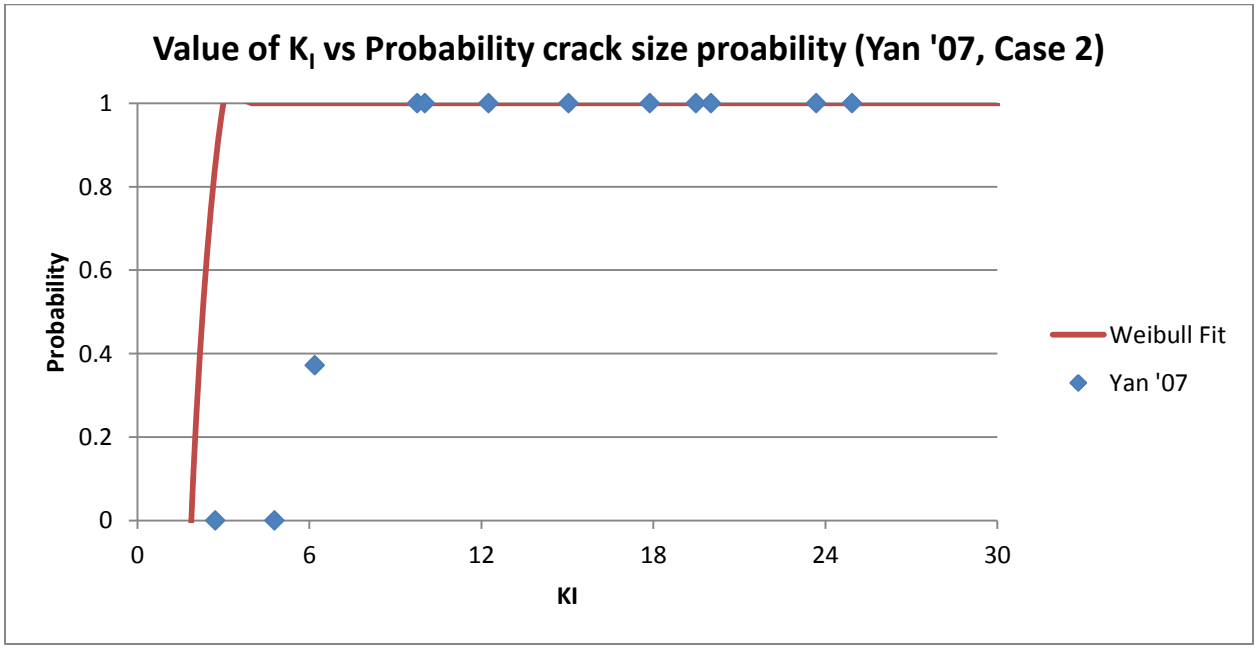

Figure 23: Weibull Probability Distribution Predicting crack length exceeding limit with respect to KI generated on beam, Yan Model, Load Case 2

The probability of a threshold crack per thickness of the specimen would also be an important piece of information.

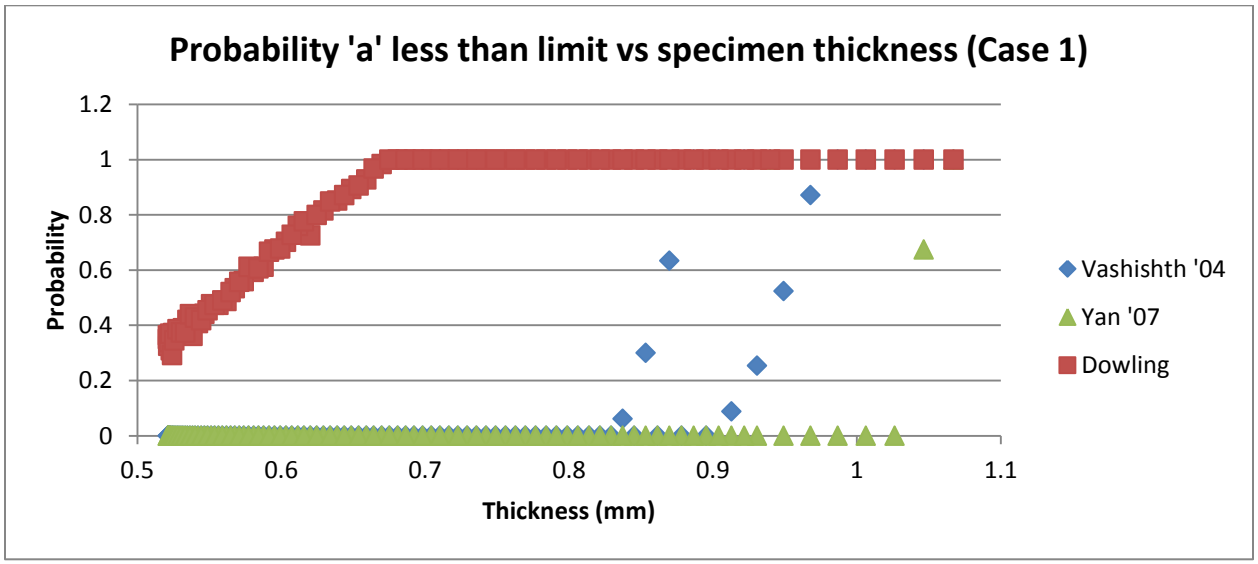

Figure 24: Probability of exceeding threshold crack vs. the thickness of the beam, Load Case 1

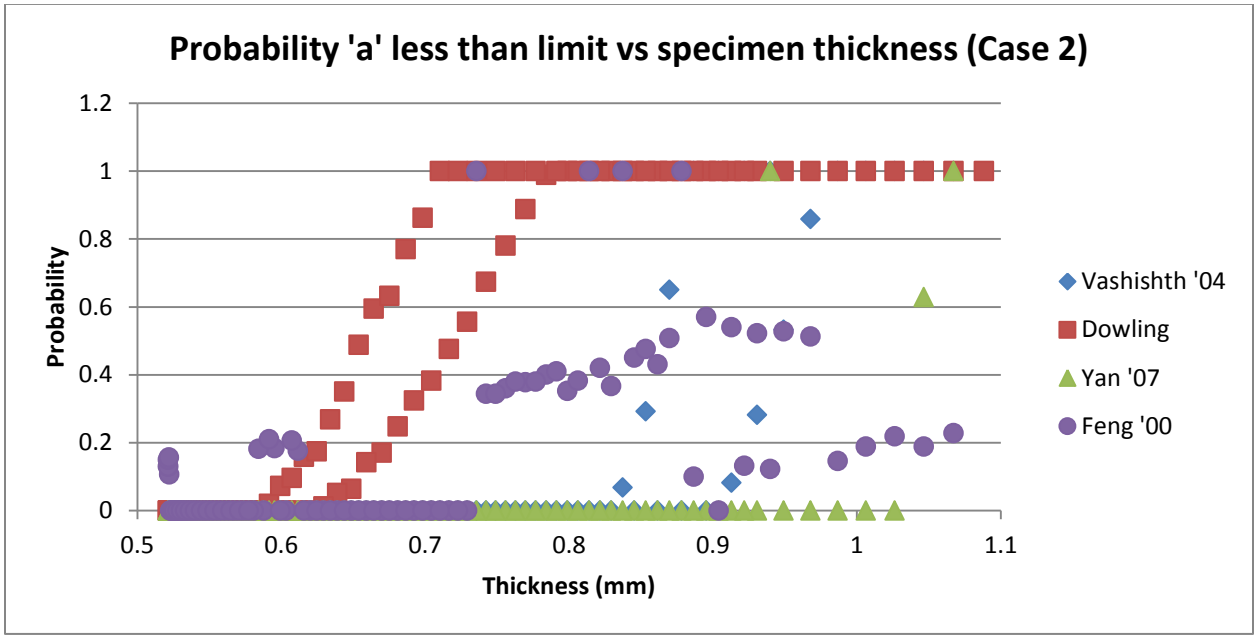

Figure 25: Probability of exceeding threshold crack vs. the thickness of the beam, Load Case 2

Figures 24 and 25 are the probability that the crack will be beneath the threshold crack. From these charts it can be seen that the Yan beam model [16] is the most likely model to have cracks above the crack threshold. From the charts from case 1 and case 2

the thickness of the model has to be greater than about 0.94 millimeters to begin to have a chance of a crack below the threshold length. The Vashishth tension model [19] has a different distribution. The threshold limit lowers to a thickness of about 0.83 mm in case 1 and 0.68 mm in case 2. The Dowling model for load case 1 has the least likely chance of fracture with a 31% chance of not surpassing the limit at the beam's thinnest point. The Feng model for load case 1 was intentionally not shown due to large outliers that skewed the data and for load case 2 the probability was irregular.

The stress intensity value has a length multiplier, in the Yan beam bending models, which represents the unsupported span. This is not realistic because the trabecular core supports the cortical shell at spans of a very short length. An adjustment was made to the multiplier to find the unsupported length that made the Yan model fall within the same range as the other models. 5.5 mm was found to be suitable and maintained the conservative values. The result was that the stress intensity at the crack tips was consistent with the other compact section models see figures 26 and 27.

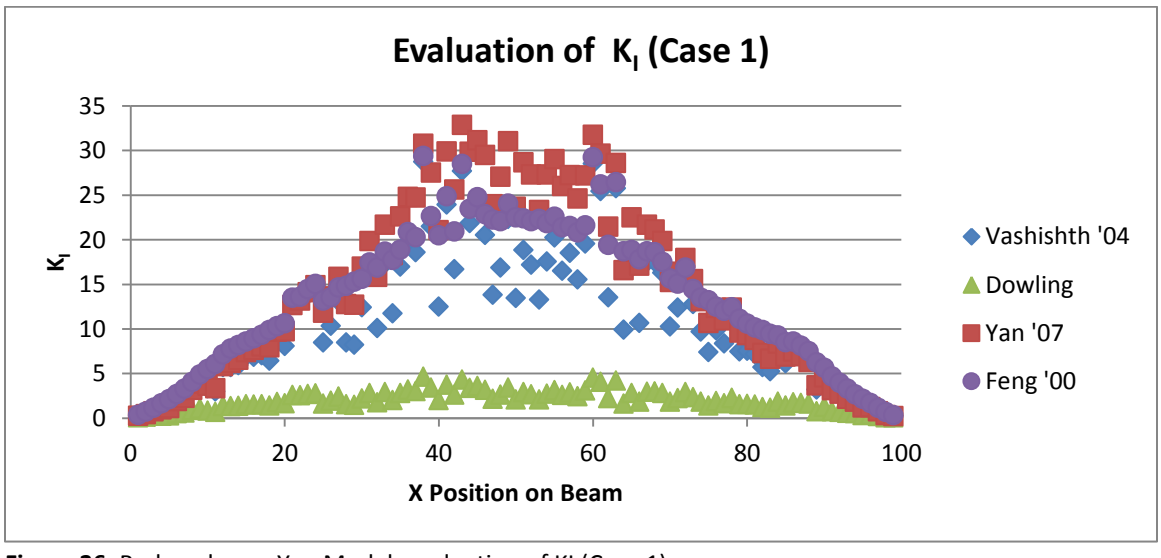

Figure 26. Reduced span Yan Model, evaluation of KI (Case 1).

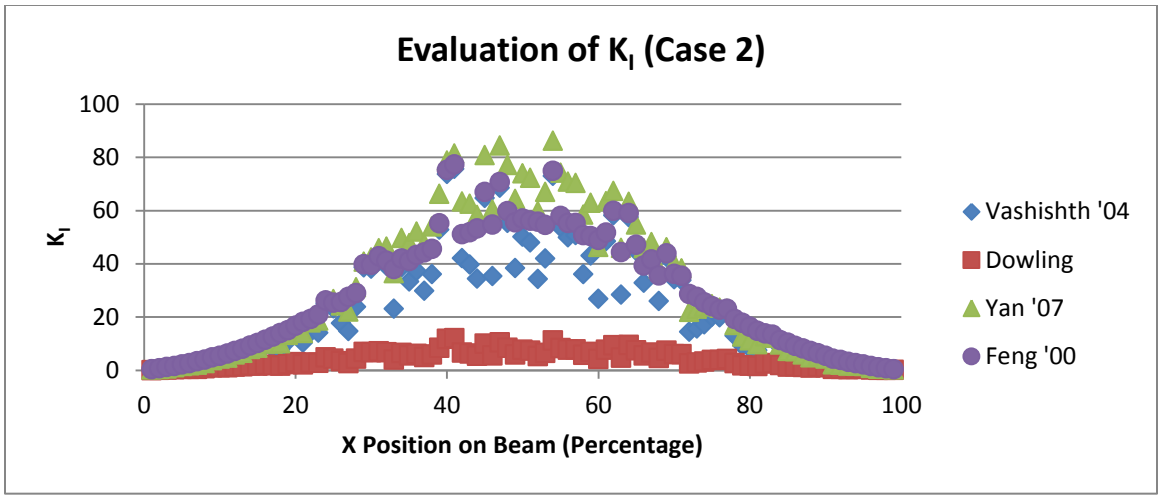

Figure 27. Reduced span Yan Model, evaluation of KI (Case 2).

Chapter IX - Conclusion

This research develops a probabilistic assessment method for determining the presence of cracks of sufficient length to fracture bone. This is important because subsidence cannot be characterized by yield mechanics of gross materials properties. This technique is needed because the porous structure of bone causes stress raisers that initiate failure before bone reaches its yield conditions.

This probabilistic model enables the ability to determine the likelihood of fracture based on the probabilistic presence of a crack in cortical bone. The work expands bone fracture research conducted by Vashishth, Feng, and Yan to a non ASTM standard model. This expanded work increases the applicability of the fracture work to areas of the body not well described by ASTM specimen size requirements. It also establishes the presence of pores that change the type of failure that is considered mechanically.

The probabilistic framework of this report makes the following assumptions:

- Cortical bone acts as an isotropic, homogenous, linear elastic material
- The endplate will behave like a beam
- The radial cortical shell provides pinned supports for the beam
- Single cracks are normally distributed
- Shape factors for compact sections apply to individual beam segments

- The shape function for the beam applies to cracks at any position x
- Uniaxial stress conditions

This research is primarily limited by ASTM size constraints. ASTM standards require certain length to width ratios, thickness to width ratios, and other size specifications that are not fully met by this model. Secondly, this model is limited by the use of compact tension models to represent the differential beam sections. This is application expands the work of Vashishth, Feng, Dowling and Yan to beam models that are different from the ASTM experiment by which the fracture values were measured.

Further research in to this topic would prove very useful. Verification is important and biomechanical tests of vertebral bone would be useful. This model is also limited to Mode I, tensile, failure. Bone is subjected to more than tensile forces. Expanding the study to consider Mode II and III fracture and the associated probabilities of fracture would improve bone strength assessments. This research does not consider the overall reduction in strength; however, it could be included in the analysis as a reduction to bending stress or deflection limits. It is also recommended to further examine the length multiplier for the Yan beam model. A shorter unsupported length would give more a representative stress intensity values per crack length.

Chapter X - References

1. Craig, Roy R. Mechanics of Materials, 2nd Ed; John Wiley & Sons, 2000; pp 448-505.
2. Hibbeler, R.C. Mechanics of Materials, 6th Ed. Pearson Prentice Hall, New Jersey, 2005; pp 263-361.
3. American Institute of Steel Construction, Inc. (AISC). Steel Construction Manual, 13th Ed.; pp. 3-212 – 3-213.
4. Montgomery, Douglas C.; Runger George C. Applied Statistics and Probability for Engineers, 4th Ed.; John Wiley & Son, New Jersey, pp 145-146.
5. Dowling, Norman E. Mechanical Behavior of Materials, Engineering Methods for Deformation, Fracture, and Fatigue 2nd Ed.; Prentice Hall, New Jersey, 1999; pp. 286-337.
6. Boos, N. Aebi, M. Spinal Disorders, Fundamentals of Diagnosis and Treatment; Springer-Verlang, Berlin Heidelberg, 2008; pp. 41-66.
7. Panjabi, M. White, A. Clinical Biomechanics of the Spine 2nd Ed.; Lippincott Williams & Wilkins, Philadelphia, 1990; pp.
8. Fazzalari N.L., Parkinson I.H., Fogg, Q.A., Sutton-Smith P. Antero-postero differences in cortical thickness and cortical porosity of T12 to L5 vertebral bodies, Joint Bone Spine (2006) 73; 293-297

9. Bell K.L., Loveridge N., Power J., Garrahan N., Meggitt B.F., Reeve J., Regional Differences in Cortical Porosity in the Fractured Femoral Neck, Bone (1999) 24; 57-64
10. Wang X., Ni Q., Determination of cortical bone porosity and pore size distribution using a low field pulsed NMR approach, Journal of Orthopaedic Research (2003) 2; 312-319
11. Wachter N.J., Augat P., Krischak G.D., Mentzel M., Kinzl L., Claes L. Prediction of Cortical Bone Porosity *IN Vitro* by Microcomputed Tomography, Clcified Tissue International (2001) 68; 38-42
12. Behiri J.C., Bonfield W. Orientation dependence of the fracture mechanics of bone, Journal of Biomechanics (1989) 22; 863-872
13. Behiri J.C., Bonfield W. Crack velocity dependence of longitudinal fracture in bone, Journal of Material Science (1980) 15; 1841-1849
14. Behiri J.C., Bonfield W. Fracture Mechanics of Bone –the effects of density, specimen thickness and crack velocity on longitudinal fracture, Journal of Biomechanics (1984) 17; 25-34
15. Vashishth D., Behiri J.C., Bonfield W. Crack Growth Resistance in Cortical Bone: Concept of Microcrack Toughening, Journal of Biomechanics (1997) 30; 763-769
16. Yan J., Mecholsky J.J., Clifton K.B. How tough is bone? Application of elastic-plastic fracture mechanics to bone, Bone (2007) 40; 479-484
17. Norman T.L., Vashishth D., Burr D.B. Fracture Toughness of Human Bone Under Tension, Journal of Biomechanics (1994) 28, 309-320

18. Feng Z., Rho J., Han S., Ziv I. Orientation and loading condition dependence of fracture toughness in cortical bone, Materials Science Engineering C (2000) 11; 41-46
19. Vashishth D. Rising crack-growth-resistance behavios in cortical bone: implications for toughness measurements, Journal of Biomechanics (2004) 37; 943-946
20. Biewener A.A. Safety Factors in Bone Strength, Calcified Tissue International(1993) 53; S69-S74
21. Mossekilde L., Vertebral Structure and Strength *In Vivo* and *In Vitro*, Calcified Tissue International (1993) 53; S121-S126
22. Rho J.Y., Tsui T.Y., Pharr G.M. Elastic properties of human cortical and trabecular lamellar bone measured by nanoindentation, Biomaterials (1997) 18; 1325-1330
23. Bayraktar H.H., Morgan E.F., Niebur G.L., Morris G.E., Wong E.K., Keaveny T.M. Comparison of the elastic and yield properties of human femoral trabecular and cortical tissue, Journal of Biomechanics (2004) 37; 27-35
24. Ulrich D., Hildebrand T., van Rietbergen B., Muller R., R-uegsegger P. The quality of trabecular bone evaluated with micro-computed tomography, fea and mechanical testing, Studies in Health Technology and Informatics (1997) 40; 97-112
25. Hou F.J., Lang S.M., Hoshaw S.J., Reimann D.A., Fyhrie D.P. Human vertebral body apparent and hard tissue stiffness. Journal of Biomechanics (1998) 31; 1009-1015

26. Ladd A.J., Kinney J.H., Haupt D.L., Goldstein S.A. Finite element modeling of trabecular bone: comparison with mechanical testing and determination of tissue modulus, Journal of Orthopedic Research (1998) 16; 622-628
27. Niebur G.L., Feldstein M.J., Yuen J.C., Chen T.J., Keaveny T.M. High Resolution finite element models with tissue strength asymmetry accurately predict failure of trabecular bone, Journal of Biomechanics (2000) 33; 1575-1583
28. Roy M., Rho J.Y., Tsui T.Y., Pharr G.M. Variation of young's modulus and hardness in human lumbar vertebrae measured by nanoindentation, In: Proceedings of the Bioengineering Conference, Atlanta, GA, ASME BED 33; 385-386
29. Turner C.H., Rho J., Takano Y., Tsui T.Y., Pharr G.M. The elastic properties of trabecular and cortical bone tissues are similar: results from two microscopic measurement techniques, Journal of Biomechanics (1998) 31, 1187-1192
30. Zysset P.K., Guo X.E., Hoffler C.E., Moore K.E., Goldstein S.A., Elastic modulus and hardness of cortical and trabecular bone lamellae measured by nanoindentation in the human femur, Journal of Biomechanics (1999) 32, 1005-1012
31. Kopperdahl D.L., Keaveny T.M. Yeild strain behavior of trabecular bone, Journal of Biomechanics (1998) 31; 601-608
32. Hansson T.H., Kelles T.S., Panjabi M.M. A study of the compressive properties of lumbar vertebral trabeculae: Effects of tissue characteristics, Spine (1987) 11; 837-844

33. Hvid I., Jenson N.C., Bunger C., Solund K., Djurhuus J.C., Bone mineral assay: Its relation to the mechanical strength of cancellous bone, Engineering Medicine (1985) 14; 79-83
34. Keaveny T.M., Wachtel E.F., Ford C.M., Hayes W.C. Differences between the tensile and compressive strengths of bovine tibial trabecular bone depend on modulus, Journal of Biomechanics (1994) 27; 1137-1146
35. Lindahl O. Mechanical properties of dried defatted spongy bone, Acta Orthepedica Scandinavia (1976) 47; 11-19
36. Mosekilde L., Danielsen C.C. Biomechanical competence of vertebral trabecular bone in relation to ash density and age in normal individuals, Bone (1987) 8, 79-85
37. Rohl L., Larsen E., Linde F., Odgaard A., Jorgensen J. Tensile and compressive properties of cancellous bone, Journal of Biomechanics (1991) 24; 1143-1149
38. Turner C.H. Yield behavior of bovine cancellous bone. Journal od Biomechanical Engineering (1989) 111; 256-260
39. Grant J.P., Oxland T.R., Dvorak M.F., Fisher C.G. The effects of bone density and disc degeneration on the structural property distributions in the lower lumbar endplates, Journal of Orthopedic Research (2002) 20; 1115-1120
40. Ordway N.R., Lu Y.M., Zhang X., Cheng C.C., Fang H., Fayyazi A.H. Correlation of cervical endplate strength with CT measured subchondral bone density, European Spine Journal (2007) 16; 2104-2109

41. Grant J.P., Oxland T.R., Dvorak M.F. Mapping the Structural Properties of the Lumbosacral Vertebral Endplates, Spine (2001) 8; 889-896
42. Muller-Gerbl M., Weiber S., Linsenmeier U. The distribution of mineral density in the cervical vertebral endplates, European Spine Journal (2008) 17; 432-438
43. Roberts s., McCall I.W., Menage J., Haddaway M.J., Eisenstein S.M. Does the thickness of the vertebral subchondral bone reflect the composition of the intervertebral disc? European Spine Journal (1997) 6; 385-389
44. Eswaran S.E., Gupta A., Adams M.F. Keaveny T.M. Cortical Load Sharing in the Human Vertebral Body, Journal of Bone and Mineral Density (2006) 21; 307-314
45. Eswaran S.E., Gupta A., Keaveny T.M. Locations of bone tissue at high risk of initial failure during compressive loading of the human vertebral body, Bone (2007) 41; 733-739
46. Eswaran S.E., Bayraktar H.H., Adams M.F., Gupta A., Hoffmann P.F., Lee D.C., Papadopoulos P., Keaveny T.M. The micro-mechanics of cortical shell removal in the human vertebral body, Computer Methods in Applied Mechanics and Engineering (2007) 196; 3025-3032
47. Hulme P.A. Boyd S.K., Ferguson S.J. Regional variation in vertebral bone morphology and its contribution to vertebral fracture strength, Bone (2007) 41; 946-957
48. Van der Houwen E.B., Baron P., Veldhuizen A.G., Burgerhof J.G.M., van Ooijen P.M.A., Verkerke G.J. Geometry of the Intervertebral Volume and Vertebral Endplates of the Human Spine, Annals of Biomedical Engineering (2010) 38;33-40

49. Langrana N.A., Kale S.P., Edwards W.T., Lee C.K., Kopacz K.J. Measurements and analyses of the effects of adjacent endplate curvatures on vertebral stresses, The Spine Journal (2006) 6; 267-278
50. Choi J.Y., Sung K.H. Subsidence after anterior lumbar interbody fusion using stand-alone rectangular cages, European Spine Journal (2006) 15; 16-22
51. Polikeit A., Ferguson S.J., Nolte L.P., Orr T.E. The importance of the Endplate for INterbody Cages in the Lumbar Spine, European Spine Journal (2003) 12; 556-561
52. Ferguson S., Steffen T. Biomechanics of the aging spine, European Spine Journal (2003) 12; S97-S103
53. Pitzen T., Schmitz B., Georg T., Barbier D., Beuter T., Steudel W.I., Reith W. Variation of endplate thickness in the cervical spine, European Spine Journal (2004) 13; 235-240
54. Edwards T.W., Zheng Y., Ferrara L.A., Yuan H.A. Structural Feature and Thickness of the Vertebral Cortex in the Thoracolumbar Spine, Spine (2001) 15; 218-225
55. Panjabi M.M., Chen N.C., Shin E.K., Wang J.L. The Cortical Shell Architecture of Human Cervical Vertebral Bodies, Spine (2001) 26; 2748-2484
56. Bogduck N. Mercer S. Biomechanics of the cervical spine. I: Normal kinematics, Clinical Biomechanics (2000) 15; 633-648
57. Seeley R.R., Stephens T.D., Tate P. Selected Material from Anatomy & Physiology, Wright State University (2009) McGraw Hill Learning Solutions

58. Penning L., Wilmink J.T. Rotation of the cervical spine. A CT study in normal subjects, Spine (1988) 3; 37-47

59. Lind B., Sihlbom H., Nordwall A., Malchau H. Normal Ranges of Motion of the cervical spine, Archives of Physical Medicine and Rehabilitation (1989) 70; 692-695

60. Dvorak J., Penning L., Hayek J., Panjabi M.M., Zehnder R.I. Functional Diagnostics of the cervical spine using computer tomography, Nueroradiology (1988) 132-137

61. Aho A, Vartiamen O, Salo, O. Segmentary antero-posterior mobility of the cervical spine, Annales Medicine Internae Fenniae (1955) 44; 287-299

62. Bhalla S.K., Simmons E.H., Normal Ranges of intervertebral joint motion of the cervical spine, Canadian Journal of Surgery (1969) 12; 181-187

63. Wheeldon J.A., Pintar F.A., Knowles S., Yoganandan N. Experimental flexion/extension data corridors for validation of finite elemnt models of the young, normal cervical spine, Journal of Biomechanics (2006) 39; 375-380

64. Galbusera F., Bellini C.M., Costa F., Assietti R., Fornari M. Anterior cervical fusion: a biomechanical comparison of 4 techniques, Journal of Nuerosurgery: Spine (2008) 9; 444-449

65. Roy M.E., Rho J.Y., Tsui T.Y., Evans N.D., Pharr G.M. Mechanical and morphological variation of the human lumbar vertebral and trabecular bone, Journal of Biomedical Materials Research Part A (1999) 44; 191-197

66. Shi X., Liu S., Wang X., GuoX. E., Niebur G.L. Effects of trabecular type and orientation on microdamage susceptibility in tarbecualar bone, Bone (2010) 46; 1260-1266

67. Adam C., Pearcy M., McCombe P. Stress analysis of interbody fusion – finite element modeling of inter-vertebral implant and vertebral body, Clinical Biomechanics (2003) 18; 265-272

68. Homminga J., Van-Rietbergen B., Lochmuller E.M., Weinans H., Eckstein F., Huiskes R. The osteoporotic vertebral structure is well adapted to the loads of daily life, but not to infrequent “error” loads, Bone (2004) 34; 510-516

69. Jost B., et. al. Compressive strength of interbody cages in the lumbar spine: the effect of cage shape, posterior instrumentation and bone density, European Spine Journal (1998) 7; 132-144

70. Van Jonbergen H.P., Spruit M., Anderson P. Anterior cervical interbody fusion with a titanium box cage: early radiological assessment of fusion and subsidence, The Spine Journal (2005) 5;645-649

71. Kulkarni A., D’Orth H., Wong H. Solis cage (PEEK) for anterior cervical fusion: preliminary radiological results with emphasis on fusion and subsidence, The Spine Journal (2007) 7; 205-209

72. Panzer M., Cronin D. C4-C5 segment finite element model development, validation, and load sharing investigation, Journal of Biomechanics (2009) 42; 480-490

73. Denoziere G., Ku D. Biomechanical comparison between fusion of two vertebrae and implantation of artificial disc, Journal of Biomechanics (2006) 39; 766-775
74. Polikeit A., et. al. Factors influencing stresses in the lumbar spine after the insertion of intervertebral cages: Finite element analysis, European Spine Journal (2003) 12; 413-420
75. Polikeit A., et. al. The importance of the endplate for interbody cages in the lumbar spine, European Spine Journal (2003) 12;556-561
76. Rohlmann A., Zander T., Bergmann G. Effects of fusion-bone stiffness on the mechanical behavior of the lumbar spine after vertebral body replacement, Clinical Biomechanics (2006) 21; 221-227
77. Li Y., Lewis G. Influence of surgical treatment for disc degeneration disease at C5-C6 on changes in some biomechanical parameters of the cervical device, Medical Engineering & Physics (2010) 32; 595-603
78. Standard Test Method for Plane-Strain Fracture Toughness of Metallic Materials. ASTM E399-90
79. Phillips C.A., Human Factors Engineering; Jon Wiley & Sons, 2000; p36
80. Behiri J.C., Bonfield W. Orientation and age-related dependence of fracture toughness of cortical bone, Biomechanics: Current Interdisciplinary Research (1985) pp.185-189
81. Bonfield W., Grynpas M.D., Young R.J. Crack velocity and the fracture of bone, Journal of Biomechanics (1978) 1; 473-479

82. Norman T.L., Vashishth D., Burr D.B. Effect of groove on bone fracture toughness, Journal of Biomechanics (1992) 25; 1489-1492

83. Wright T.M., Hayes W.C. Fracture mechanics parameters for compact bone – effects of density and specimen thickness, Journal of Biomechanics (1977) 10; 419-430

84. Roberts S., McCall I.W., Menage J., Haddaway M.J., Eisenstein S.M. Does the thickness of the vertebral subchondral bone reflect the composition of the intervertebral disc?, European Spine Journal (1997) 6; 385-389

85. Susan Hueston, Matt Binkley MD, and Tarun Goswami D.Sc. Statistical Analysis of Dimensional anatomy of the vertebral bodies of the Cervical Spine. Pending Publication Upon Review

Chapter XI - Appendix

Calculations

Determination of thickness of the bone beam model as function of length of the beam:

$$y = 0.0002x^2 - 0.0013x + 0.5234$$

Where:

y = beam thickness

x = the length along the beam

The moment calculated per length of the beam is as follows (AISC 13th Edition):

Case 1: (Two Equal Concentrated Loads Symmetrically Placed)
(for x less than a)

$$M(x) = P \cdot x$$

Where:

M = The applied moment

P = Applied point load

(for x greater than a)

$$M(x) = P \cdot a$$

Where:

a = the distance from the end of the beam to the point of load application

Case 2: (Uniform Load Partially Distributed)

(for x less than a)

$$M(x) = \frac{wbx}{2l}(2a + b)$$

Where:

w = The applied uniform load

b = The length of the applied uniform load

l = The length of the beam

(for x greater than a)

$$M(x) = \frac{wbx}{2l}(2a + b) - \frac{w}{2}(x - a)^2$$

The moment of inertia per length of the rectangular beam model was calculated as follows (Hibbeler 2005):

$$I = \frac{bh^3}{12}$$

Where:

b = The base width of the beam

h = The thickness of the beam

I = The moment of inertia

The stress in the tension fiber of the beam was calculated as follows (Hibbeler 2005):

$$\sigma = \frac{Mh}{2I}$$

Where:

σ = The stress applied to the beam

Probabilistic cracks were inserted into the beam at a spacing of .2 millimeters. The crack size was determined from a normal distribution calculated as described earlier. The distribution was truncated with a maximum and minimum. The flowing table is the information used to build the distribution.

Normal Distribution Parameter Values (mm)			
Average	Standard Deviation	Minimum	Maximum
.1590	.1778	.0628	.3592

Table 15: Data used to build normal distribution

The following diagram is a histogram of the normal distribution. The sample size for each distribution is 500.

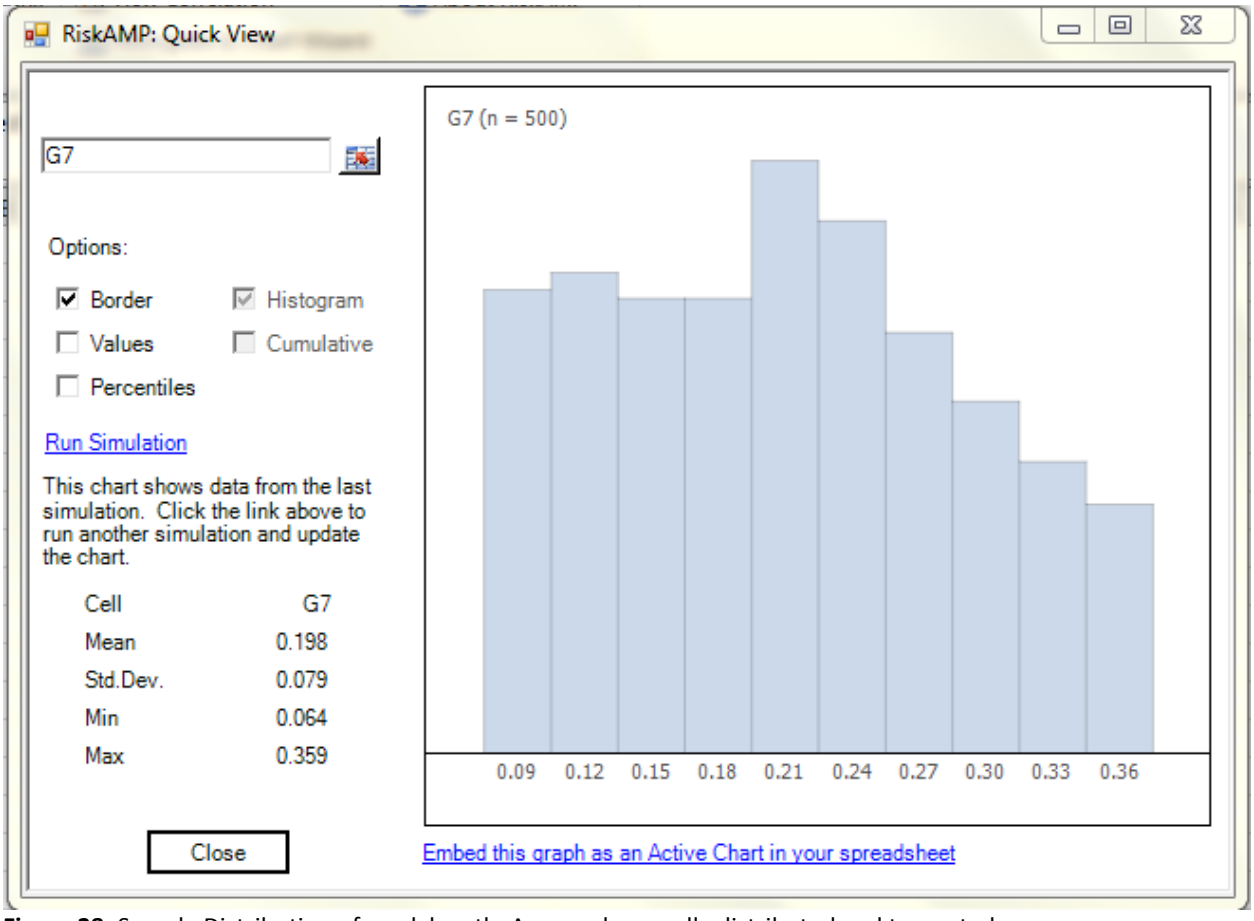

Figure 28: Sample Distribution of crack length, Assumed normally distributed and truncated.

From the distribution of crack sizes denoted as ‘a’ was used to determine the fracture toughness of the bone at the spot of interest. The fracture toughness was calculated with the following equation:

$$K_{Ic} = \frac{P_q Y}{(BB_n)^{1/2} W^{1/2}}$$

Where:

K_{Ic} = The fracture toughness of the specimen

P_q = The moment applied at the point of interest

Y = Shape function

B = Thickness of the specimen

B_n = Reduced thickness of the specimen at the placement of the crack

W = The distance from point of load application to the opposite end of the specimen

Four models were compared for the fracture toughness of a specimen. The fracture toughness was calculated the same way for each model with the exception of the last model which was based on a three point bend. The equation for the three point bending determination of fracture toughness is as follows:

$$K_{Ic} = \frac{SP_q Y}{(BB_n)^{1/2} W^{1/2}}$$

Where:

S = The span of the beam between supports

Four shape functions were modeled and compared to examine the effects on the fracture toughness. The four shape models are as follows:

$$Y = \frac{3\alpha^{1/2}[1.99 - \alpha(1-\alpha)*(2.15 - 3.93\alpha + 2.7\alpha^{2)}]}{2(1+2\alpha)*(1-\alpha)^{1/2}}$$ (ASTM E399, A3.2)

$$\alpha = \frac{a}{W}$$

$$Y = \frac{(2+\frac{a}{W})}{(1-\frac{a}{W})^{3/2}}\{.866 + 4.64(\frac{a}{W}) - 13.36(\frac{a}{W})^2 + 14.72(\frac{a}{W})^3 - 5.6(\frac{a}{W})^4\}$$ (ASTM E399, A4.2)

$$Y = 29.6(\frac{a}{W})^{1/2} - 185.5(\frac{a}{W})^{3/2} + 655.7(\frac{a}{W})^{5/2} - 1017(\frac{a}{W})^{7/2} + 638.9(\frac{a}{W})^{9/2}$$ (Norman 95, Feng 00)

$$Y = \sqrt{\frac{2}{\pi a}\tan\left(\frac{\pi a}{2}\right)}\left[\frac{.923 + .199\left(1 - \sin\left(\frac{\pi a}{2}\right)\right)}{\cos\left(\frac{\pi a}{2}\right)}\right]$$ (Dowling 1999)

The first three models have been used previously in research. The last model was developed from a textbook formula (Dowling 1999) to judge a comparison that was not used for bone.

The applicability of linear elastic fracture mechanics had to be checked at each point along the beam. The equation used to check for LEFM applicability was:

$$a, (b-a), h \geq \frac{4}{\pi}\left(\frac{K}{\sigma_o}\right)^2$$

It is also necessary to check to see if the specimen is in plane strain or plane stress. That can be done using the following equation:

$$a, (b-a), h \geq 2.5\left(\frac{K}{\sigma_o}\right)^2$$

All points on the beam were LEFM applicable and plane stress applied to the entire beam as well. At this point an excel function goal seek was used to adjust the crack size 'a' so that the fracture toughness K was at a limit state determined from research. Once this was accomplished the crack length was compared to the normal distribution previously developed. A function available through the monte carlo plugin SimulationInterval was used to determine the probability of the limit a random crack length 'a' being less than the limit crack length. This was then used to develop the distribution charts.

After the probabilities were found for the crack size being under the limiting crack size the data was analyzed with a Weibull continuous distribution function. The Weibull CDF is as follows:

$$f(x) = 1 - e^{-\left(\frac{x}{\delta}\right)^{\beta}}$$

Where:

x = The nonlimited value of K along the beam

β = the standard deviation reciprocal of all the probability data along the length of the beam

δ = the exponential average of all the probability data along the length of the beam

The Weibull distribution was used to determine an equation to find the probability of an crack along the length of the beam. To determine the quality of the Weibull distribution an R^2 value was determined for each plot.